Euro. Jnl of Applied Mathematics (2015), *vol.* 26, *pp.* 671–719.
doi:10.1017/S0956792515000364

On contact-line dynamics with mass transfer

J. M. OLIVER[1], J. P. WHITELEY[2], M. A. SAXTON[1], D. VELLA[1], V. S. ZUBKOV[1] and J. R. KING[3]

[1]*Mathematical Institute, University of Oxford, Andrew Wiles Building, Radcliffe Observatory Quarter, Woodstock Road, Oxford, OX2 6GG, UK*
Email: oliver@maths.ox.ac.uk, saxton@maths.ox.ac.uk, vella@maths.ox.ac.uk, zubkov@maths.ox.ac.uk
[2]*Department of Computer Science, University of Oxford, Parks Road, Oxford, OX1 3QD, UK*
Email: jonathan.Whiteley@cs.ox.ac.uk
[3]*School of Mathematical Sciences, University of Nottingham, Nottingham NG7 2RD, UK*
Email: John.King@nottingham.ac.uk

(*Received 6 March 2015; revised 8 June 2015; accepted 23 June 2015; first published online 10 August 2015*)

We investigate the effect of mass transfer on the evolution of a thin, two-dimensional, partially wetting drop. While the effects of viscous dissipation, capillarity, slip and uniform mass transfer are taken into account, other effects, such as gravity, surface tension gradients, vapour transport and heat transport, are neglected in favour of mathematical tractability. Our focus is on a matched-asymptotic analysis in the small-slip limit, which reveals that the leading-order outer formulation and contact-line law depend delicately on both the sign and the size of the mass transfer flux. This leads, in particular, to novel generalisations of Tanner's law. We analyse the resulting evolution of the drop on the timescale of mass transfer and validate the leading-order predictions by comparison with preliminary numerical simulations. Finally, we outline the generalisation of the leading-order formulations to prescribed non-uniform rates of mass transfer and to three dimensions.

Key words: Thin films, surface-tension driven flows, evaporation, condensation, matched asymptotic expansions.

1 Introduction

Mathematical formulations for, or equivalent to those for, the evaporation and condensation of a sessile liquid drop are of practical importance in numerous geophysical, biomedical and industrial applications including the water cycle, DNA mapping and gene-expression analysis, biofilm growth, the manufacturing of semiconductor and micro-fluidic devices, cooling, coating, patterning and condensing; see, for example, [3, 6, 29–32, 35, 41] and references therein. The free-boundary problem is complicated because of the need to consider the transport of mass, momentum and energy within and between the substrate, the liquid drop and the atmosphere around the drop [31]. If the drop is partially wetting, the problem is compounded by the singularities that may arise in the state variables at the contact line, notably the stress singularity in the liquid [22] and a singularity in the evaporative flux when evaporation is limited by the diffusion of vapour into the surrounding atmosphere [8, 9]. Theoretical efforts have focussed most extensively on numerical simulations in the thin-film regime in which it is possible to derive tractable models that incorporate many of the pertinent thermo- and hydro-dynamical effects; see, for

example, [1,2,4,10–12,15,20,27,33,38] and references therein. However, the simplifications and physical insight afforded by a systematic asymptotic analysis are less prevalent in the literature. For example, [28] states that: *"New asymptotic methods will also need to be developed to connect the nano-scale of relevance to the contact line physics and the macro-scale of a drop."* A particularly well-studied regime is the "one-sided" model in which vapour is transported away from the drop sufficiently rapidly that it does not affect the evaporative flux [4,6,28]. In the resulting thin-film models [28] describe how the evaporative flux may be weakly dependent on the film thickness, i.e. nearly constant. This work motivates the present study, though we emphasise that in most practical applications the evaporative flux is much smaller than the values considered in this paper, so that our analysis focusses on putting in context the physically relevant case and developing the methodology required to analyse such challenging thin-film problems. We note that larger rates of mass transfer may be relevant under extreme conditions in the evaporation or condensation of a sessile liquid drop, and are relevant in other related applications, including the spreading of a viscous liquid on a porous substrate described in, for example, [7] and references therein. They are also relevant in other contexts, such as in thin-film models for cell motility and biofilm growth of the type described in, for example, [25,41].

In this paper, we consider the effect of the simplest possible mass-transfer mechanism on the simplest possible two-dimensional model for the contact-line dynamics of a thin drop of viscous liquid partially wetting a rigid, flat, impermeable substrate. We consider the isothermal regime in which the density, viscosity, surface tension, static contact angle and mass transfer flux are constant and the liquid slips on the substrate according to a generalised Navier slip law. We neglect the effects of, *inter alia*, gravity, surface tension gradients, vapour recoil and vapour transport. In Section 2, we formulate and nondimensionalise the thin-film problem. In Sections 3–4, we use the method of matched asymptotic expansions to analyse the small-slip limit in the two pertinent distinguished limits, which can be viewed as corresponding to the rate of mass transfer being small and large, respectively. In Sections 5–6, we use a combination of analytical and numerical methods to investigate the leading-order formulations that are selected in the small-slip limit. In Section 7, we summarise our results, discuss directions for future work and outline the straightforward generalisation of the small-slip asymptotics to non-uniform rates of mass transfer and to three dimensions.

2 Formulation

We consider the motion of a two-dimensional viscous drop partially wetting a rigid, flat, impermeable substrate. Introducing Cartesian coordinates (x^*, y^*) measuring distance tangential and normal to the substrate, respectively, we denote by $y^* = h^*(x^*, t^*)$ the free surface of the drop, where t^* is time. Here and hereafter, starred variables denote dimensional quantities. For simplicity, we assume that the flow is symmetric about $x^* = 0$ and consider the evolution of the liquid in $0 < y^* < h^*(x^*, t^*)$, $0 < x^* < s^*(t^*)$, where $x^* = s^*(t)$ denotes the *a priori* unknown location of the right-hand contact line at which the drop thickness $h^* = 0$. In addition we assume that: the liquid flow is incompressible and governed by the Stokes equations, with constant viscosity μ and no external body forces; the drop loses mass through its free boundary at a constant area flux J^* per unit

https://doi.org/10.1017/S0956792515000364 Published online by Cambridge University Press

length per unit time; the traction on the free surface is due to a constant surface tension γ only; the liquid slips on the substrate according to a slip law with slip length $\Lambda(h^*)^{n-2}$, where Λ and n are parameters (we shall see that $n < 3$ is required for contact line motion); the microscopic contact angle Φ between the free boundary and substrate is constant and small; there is no flux of liquid through the contact line; the initial drop profile is smooth and has a small aspect ratio of the order of Φ.

Denoting the liquid velocity and pressure by (u^*, v^*) and p^*, respectively, a standard lubrication analysis in the small-Φ limit results at leading order in the lubrication equations (see, for example, [29, 30])

$$\mu \frac{\partial^2 u^*}{\partial y^{*2}} = \frac{\partial p^*}{\partial x^*}, \ \frac{\partial p^*}{\partial y^*} = 0, \ \frac{\partial u^*}{\partial x^*} + \frac{\partial v^*}{\partial y^*} = 0 \text{ for } 0 < y^* < h^*(x^*, t^*),$$

together with the generalised-slip and no-flux boundary conditions on the substrate,

$$u^* = \Lambda(h^*)^{n-2} \frac{\partial u^*}{\partial y^*}, \ v^* = 0 \text{ on } y^* = 0,$$

and the kinematic and dynamic boundary conditions on the free surface,

$$v^* = \frac{\partial h^*}{\partial t^*} + u^* \frac{\partial h^*}{\partial x^*} + J^*, \ p^* = -\gamma \frac{\partial^2 h^*}{\partial x^{*2}}, \ \frac{\partial u^*}{\partial y^*} = 0 \text{ on } y^* = h^*(x^*, t^*).$$

We then obtain in the usual way the expressions

$$\frac{\partial h^*}{\partial t^*} = \frac{\partial}{\partial x^*} \left(\left(\frac{h^{*3}}{3\mu} + \frac{\Lambda h^{*n}}{\mu} \right) \frac{\partial p^*}{\partial x} \right) - J^*, \ p^* = -\gamma \frac{\partial^2 h^*}{\partial x^{*2}} \text{ for } 0 < x^* < s^*(t^*),$$

governing the evolution of the film thickness $h^*(x^*, t^*)$ and the pressure $p^*(x^*, t^*)$.

Denoting by $2L$ the initial width of the drop, so that $s^*(0) = L$, we nondimensionalise by scaling $x^* = Lx$, $t^* = 3\mu L t/(\Phi^3 \gamma)$, $s^* = Ls$, $p^* = \gamma \Phi p/L$ and $h^* = \Phi L h$ to obtain the dimensionless thin-film equation

$$\frac{\partial h}{\partial t} + \frac{\partial}{\partial x} \left(\left(h^3 + \lambda^{3-n} h^n \right) \frac{\partial^3 h}{\partial x^3} \right) = -J \text{ for } 0 < x < s(t), \tag{2.1}$$

where we have eliminated the pressure $p = -\partial^2 h/\partial x^2$, and the dimensionless slip length λ and mass transfer flux J are given by

$$\lambda = \frac{(3\Lambda)^{1/(3-n)}}{\Phi L}, \ J = \frac{3\mu J^*}{\Phi^4 \gamma},$$

with mass loss and gain corresponding to $J > 0$ and $J < 0$, respectively. As described by, for example, [17, 18, 24, 40], slip laws with $n = 1$ and $n = 2$ have been widely used to both facilitate and study contact-line motion.

The modelling assumptions listed above imply that the pertinent boundary conditions for equation (2.1) are given by

$$\frac{\partial h}{\partial x} = 0, \ \frac{\partial^3 h}{\partial x^3} = 0 \text{ at } x = 0; \quad h = 0, \ -\frac{\partial h}{\partial x} = 1, \ h^n \frac{\partial^3 h}{\partial x^3} = 0 \text{ at } x = s(t)^-. \tag{2.2a-e}$$

https://doi.org/10.1017/S0956792515000364 Published online by Cambridge University Press

Near to the line of symmetry, equations (2.1) and (2.2*a*,*b*) imply that the local expansion is given by $h \sim A_1 + A_2 x^2$ as $x \to 0$, where $A_1(t)$ and $A_2(t)$ are degrees of freedom in the sense that they are globally, rather than locally, determined. Near to the contact line a local analysis of equation (2.1) subject to the boundary conditions (2.2*c*,*d*) in a frame moving with the contact line implies that $h \sim (s-x) + \hat{h}$ as $x \to s^-$, with

$$-\dot{s}(s-x) + \lambda^{3-n}(s-x)^n \frac{\partial^3 \hat{h}}{\partial x^3} \sim J(s-x) + Q \text{ as } x \to s^-, \tag{2.3}$$

where $Q(t)$ is the flux of liquid through the contact line and we have integrated once with respect to x. However, at this stage we have not yet applied the no-flux condition (2.2*e*) to set $Q = 0$ in order to make the following technical point: it follows from equation (2.3) that, for $2 \leqslant n < 3$, the local expansion for h can only be asymptotic (with $\hat{h} = \mathrm{o}(s-x)$ as $x \to 0^-$) if $Q = 0$; thus, the no-flux condition (2.2*e*) is in fact redundant for $2 \leqslant n < 3$ and need only be imposed for $n < 2$. Setting $Q = 0$ for all $n < 3$, we can now use equation (2.3) to deduce that the local expansion is given by

$$h \sim (s-x) + \begin{cases} A_3(s-x)^2 + C(s-x)^{4-n} & \text{for } n < 2, \\ \left(-\dfrac{1}{2\lambda}(\dot{s}+J)\ln(s-x) + A_3\right)(s-x)^2 & \text{for } n = 2, \\ C(s-x)^{4-n} + A_3(s-x)^2 & \text{for } 2 < n < 3 \end{cases} \tag{2.4}$$

as $x \to s^-$, where $A_3(t)$ and $s(t)$ are the only degrees of freedom and $C(t)$ is given by

$$C = \frac{\dot{s} + J}{(n-2)(n-3)(n-4)\lambda^{3-n}}. \tag{2.5}$$

It follows that the free-boundary problem (2.1)–(2.2) is correctly specified because the order of equation (2.1) is equal to the total number of degrees of freedom in the local expansions of h at $x = 0$ and $x = s(t)$ (namely $A_1(t)$, $A_2(t)$, $A_3(t)$ and $s(t)$). Moreover, the local expansion (2.4) at the contact line gives two important results: firstly, a moving boundary condition for $s(t)$ can be expressed in the form

$$\dot{s} = -J + \lim_{x \to s^-} \lambda^{3-n} h^{n-1} \frac{\partial^3 h}{\partial x^3}; \tag{2.6}$$

and, secondly, the pressure gradient at the contact line is zero for $n < 1$, finite for $n = 1$ and unbounded for $1 < n < 3$. We shall take general $n < 3$ in our asymptotic analysis of the small-slip limit of equations (2.1)–(2.2) in Sections 3–4 and $n = 1$ in our numerical simulations of equations (2.1)–(2.2) in Sections 5–6.

The problem is closed by prescribing an initial condition of the form

$$h(x,0) = \mathcal{H}(x) \text{ on } 0 < x < s(0) = 1, \tag{2.7}$$

and we shall only consider those initial profiles $\mathcal{H}(x)$ that are smooth and positive for $0 \leqslant x < 1$ and satisfy the boundary conditions (2.2). We note that integrating equation (2.1) from $x = 0$ to $x = s(t)$ and applying the zero flux conditions (2.2*b*,*e*) implies that the

https://doi.org/10.1017/S0956792515000364 Published online by Cambridge University Press

expression representing global conservation of mass is given by

$$\frac{\mathrm{d}m}{\mathrm{d}t} = -Js, \quad m(t) = \int_0^{s(t)} h\,\mathrm{d}x, \tag{2.8}$$

where $m(t)$ is the cross-sectional area of the drop in $x > 0$ at time t, and we shall donate by M the initial area at time $t = 0$, so that $m(0) = M$.

For $J > 0$ the cross-sectional area of the drop decreases monotonically with time t until it vanishes at the extinction time, which we denote by t_c. We aim to determine in the small-slip limit the dependence of the extinction time t_c on the value of $J > 0$ and on the initial profile $\mathcal{H}$, as well as any universal scaling behaviour exhibited by the drop profile $h(x, t)$ and half-drop width $s(t)$ as $t \to t_c^-$. For $J < 0$ the cross-sectional area of the drop increases monotonically with t, and we aim to determine in the small-slip limit any universal scaling behaviour exhibited by $h(x, t)$ and $s(t)$ as $t \to +\infty$. We begin in the next section with the small-slip asymptotics in the distinguished limit corresponding to small mass transfer.

3 Small-slip asymptotics with small mass transfer

In the regime in which $J = 0$ and $n = 2$, both Hocking [19] and Lacey [26] show that, at leading order on the slow timescale $T = \epsilon t = \mathrm{O}(1)$, where $\epsilon \equiv 1/\ln(1/\lambda) \to 0$ as $\lambda \to 0$, surface tension drives the drop toward a quasi-stationary steady state in which the mean curvature, and hence the pressure, are uniform (at leading order in the thin-film limit). While this result is shared by both [19] and [26], their matched-asymptotic analyses in the limit $\lambda \to 0$ are different: the spatial asymptotic structure comprises three regions in [19] and two regions in [26]. In both analyses there is an outer region in which x, $h = \mathrm{O}(1)$ and an inner region of size of $\mathrm{O}(\lambda)$ near the contact line, while [19] introduces an intermediate region between the inner and outer regions (as illustrated in Figure 1) in order to accomplish more efficiently the matching of the contact angles between them (as described in the caption to Figure 1 and about which more shortly).

In this section, we consider the distinguished limit in which mass transfer occurs on the same slow timescale by setting $\mathcal{J} \equiv J/\epsilon = \mathrm{O}(1)$ as $\lambda \to 0$. In the small-slip limit it is remarkable that the spatial asymptotic structure is exactly the same as when $J = 0$ and $n = 2$. We will begin by generalising [26] to take account of mass transfer and the generalised slip law, before moving on to reconcile this analysis with the appropriate generalisation of that in [19].

3.1 Outer region

We begin with the outer region by setting $s(t) = S(T)$, the leading-order outer balance in equation (2.1) then being quasi-steady on the timescale $T = \epsilon t = \mathrm{O}(1)$ as $\lambda \to 0$: expanding $h \sim h_0$ and $S \sim S_0$ as $\lambda \to 0$ gives

$$\frac{\partial^2 h_0}{\partial x^2} = -P_0 \text{ for } 0 < x < S_0, \tag{3.1}$$

https://doi.org/10.1017/S0956792515000364 Published online by Cambridge University Press

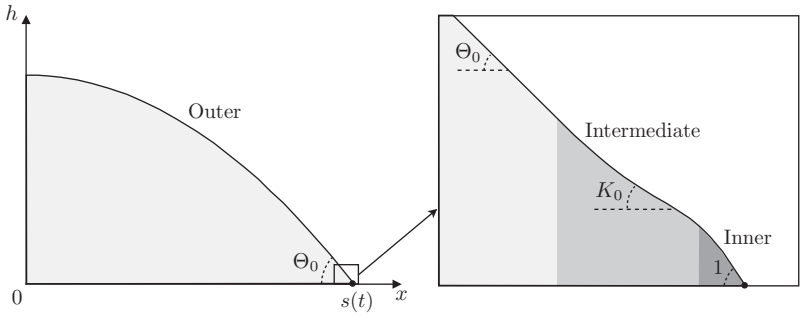

FIGURE 1. Schematic of the free-surface profile showing the outer, intermediate and inner regions in the small-slip limit in which $\lambda \to 0$; Θ_0, K_0 and 1 are the leading-order "macroscopic" (outer region), "mesoscopic" (intermediate region) and "microscopic" (inner region) contact angles, respectively; see text for details of the scalings.

with

$$\frac{\partial h_0}{\partial x} = 0 \text{ at } x = 0; \quad h_0 = 0, \ -\frac{\partial h_0}{\partial x} = \Theta_0 \text{ at } x = S_0^-, \tag{3.2}$$

where the leading-order pressure $P_0(T)$ and macroscopic contact angle $\Theta_0(T)$ have yet to be determined. Integrating equation (3.1) and applying the boundary conditions (3.2) then gives

$$h_0 = \frac{P_0}{2}\left(S_0^2 - x^2\right), \ P_0 = \frac{\Theta_0}{S_0}. \tag{3.3}$$

Substituting these expressions into the leading-order version of the expression (2.8) representing global conservation of mass gives

$$\frac{\mathrm{d}}{\mathrm{d}T}\left(\frac{S_0^2\Theta_0}{3}\right) = -\mathcal{J}S_0, \tag{3.4}$$

an ordinary differential equation that may also be derived as the solvability condition for the $\mathrm{O}(\epsilon)$ outer problem. A second ordinary differential equation relating S_0 and Θ_0 is determined by matching with the inner region, as we shall now describe.

3.2 Inner region

In the inner region the scalings $x = s + \lambda X$, $h = \lambda H$ are required both to retain slip and to match with the outer solution. The thin-film equation (2.1) becomes

$$\lambda\epsilon\frac{\partial H}{\partial T} - \epsilon\dot{S}\frac{\partial H}{\partial X} + \frac{\partial}{\partial X}\left(\left(H^3 + H^n\right)\frac{\partial^3 H}{\partial X^3}\right) = -\epsilon\mathcal{J} \text{ for } X < 0, \tag{3.5}$$

where we recall that $\epsilon = 1/\ln(1/\lambda) \to 0$ as $\lambda \to 0$. Expanding

$$H(X,T) \sim \sum_{i=0}^{\infty}\epsilon^i H_i(X,T), \quad S(T) \sim \sum_{i=0}^{\infty}\epsilon^i S_i(T) \text{ as } \lambda \to 0, \tag{3.6}$$

https://doi.org/10.1017/S0956792515000364 Published online by Cambridge University Press

the thin-film equation (3.5) implies that the evolution of H_0 is quasi-steady, with

$$\left(H_0^3 + H_0^n\right) \frac{\partial^3 H_0}{\partial X^3} = 0 \text{ for } X < 0, \tag{3.7}$$

where we have integrated once with respect to X and applied the leading-order version of the no-flux boundary condition (2.2*e*). Applying the boundary conditions (2.2*c*,*d*) and matching below with the outer region results in the boundary conditions

$$H_0 = 0, \; -\frac{\partial H_0}{\partial X} = 1 \text{ at } X = 0^-; \quad H_0 \sim A_0(T)(-X) \text{ as } X \to -\infty, \tag{3.8}$$

where $A_0(T)$ is a degree of freedom belonging to the leading-order inner problem (3.7)–(3.8) whose unique solution is simply given by $H_0 = -X$, so that $A_0 = 1$.

At $O(\epsilon^i)$, where i is a positive integer, the thin-film equation (3.5) and no-flux boundary condition (2.2*e*) imply that H_i is governed by the quasi-steady thin-film equation

$$-\sum_{j=0}^{i-1} \dot{S}_j H_{i-j-1} + \sum_{j=1}^{i} M_{i-j} \frac{\partial^3 H_j}{\partial X^3} = -\mathcal{J}\delta_{i1} X \text{ for } X < 0, \tag{3.9}$$

where $\delta_{i1} = 1$ for $i = 1$, $\delta_{i1} = 0$ for $i \geqslant 2$, and the generalised-binomial and multinomial theorems imply that the mobility M_m for integer $m \geqslant 0$ may be expressed in the form

$$M_m = \sum_{\substack{k_1,k_2,k_3 = 0 : \\ k_1+k_2+k_3 = m}}^{m} H_{k_1} H_{k_2} H_{k_3} + \sum_{k=0}^{\infty} \sum_{\substack{k_1,\ldots,k_m = 0 : \\ k_1+k_2+\cdots+k_m = k, \\ k_1+2k_2\cdots+mk_m = m}}^{k} \binom{n}{k} \binom{k}{k_1,\ldots,k_m} H_0^n \left(\frac{H_1}{H_0}\right)^{k_1} \cdots \left(\frac{H_m}{H_0}\right)^{k_m};$$

we note that $M_0 = H_0^3 + H_0^n$. Applying the boundary conditions (2.2*c*,*d*) and matching below with the outer region results in the boundary conditions

$$H_i = 0, \; -\frac{\partial H_i}{\partial X} = 0 \text{ at } X = 0^-; \quad H_i \sim A_i(T)(-X)\ln^i(-X) \text{ as } X \to -\infty, \tag{3.10a-c}$$

where $A_i(T)$ will shortly be determined by matching.

For $n < 3$, we find that the far-field expansions (3.10*c*) are consistent with the quasi-steady thin-film equations (3.9) for non-negative integers less than or equal to i provided

$$-\dot{S}_0 A_{i-1} + \sum_{j=1}^{i} \left(\sum_{\substack{k_1,k_2,k_3 = 0 : \\ k_1+k_2+k_3 = i-j}}^{i-j} A_{k_1} A_{k_2} A_{k_3} \right) j A_j = \mathcal{J}\delta_{i1}. \tag{3.11}$$

Continuing to follow closely [26], we multiply equation (3.11) by ξ^{i-1} and sum the

https://doi.org/10.1017/S0956792515000364 Published online by Cambridge University Press

resulting expressions from $i = 1$ to ∞ to find that the generating function,

$$K_0(\xi, T) = \sum_{k=0}^{\infty} A_k(T)\xi^k, \tag{3.12}$$

satisfies the first-order nonlinear differential equation

$$-\dot{S}_0 K_0 + K_0^3 \frac{\partial K_0}{\partial \xi} = \mathcal{J}, \tag{3.13}$$

as well as the boundary condition

$$K_0(0, T) = A_0(T) = 1. \tag{3.14}$$

Writing the inner solution in outer variables and expanding as $\lambda \to 0$ with $S - x = \mathrm{O}(1)$ gives

$$\lambda H\big((S-x)/\lambda, T\big) \sim \sum_{k=0}^{\infty} \epsilon^k A_k(T)(S-x)\ln^k\left(\frac{S-x}{\lambda}\right) \sim (S_0 - x)\sum_{k=0}^{\infty} A_k(T),$$

an infinite number of terms jumping order because $\epsilon = 1/\ln(1/\lambda)$. Since the local expansion of the leading-order outer solution (3.3) is given by $h_0 \sim \Theta_0(S_0 - x)$ as $x \to S_0^-$, matching implies that the generating function $K_0(\xi, T)$ also satisfies the boundary condition

$$K_0(1, T) = \sum_{k=0}^{\infty} A_k(T) = \Theta_0(T). \tag{3.15}$$

We note that it is this matching that identifies $\epsilon = 1/\ln(1/\lambda)$ as the correct choice in the expansions (3.6), the analysis in this section holding up until equation (3.14) for any small parameter ϵ satisfying the condition that $\lambda \ll \epsilon^N$ as $\lambda \to 0$ for each positive integer N.

We will show in Section 3.3 that the generating function $K_0(\xi, T)$, and hence its coefficients $A_i(T)$, are uniquely determined by the two point boundary value problem (3.13)–(3.15) whose associated consistency condition determines uniquely, but not explicitly, the leading-order contact-line velocity $\dot{S}_0$ as a function of the leading-order macroscopic contact angle Θ_0 and the rate of mass transfer $\mathcal{J}$. We denote the resulting contact-line law by

$$\dot{S}_0 = \mathcal{V}(\Theta_0, \mathcal{J}), \tag{3.16}$$

where $\mathcal{V}$ is determined in Section 3.3 via the transcendental equation (3.21).

First, however, we note that an understanding of the physical significance of the generating function $K_0(\xi, T)$ may be gained by observing that the expansion of the inner solution as $\lambda \to 0$ with

$$\xi = \epsilon \ln\left(\frac{S-x}{\lambda}\right) = \mathrm{O}(1), \tag{3.17}$$

is given by

$$\lambda H\big((S-x)/\lambda, T\big) \sim \sum_{k=0}^{\infty} \epsilon^k A_k(T)(S-x)\ln^k\left(\frac{S-x}{\lambda}\right) \equiv (S-x)K_0(\xi, T). \tag{3.18}$$

https://doi.org/10.1017/S0956792515000364 Published online by Cambridge University Press

Since equation (3.17) is equivalent to the scaling $S - x = \lambda^{1-\xi}$, it follows from equation (3.18) that the generating function $K_0(\xi, T)$ is the leading-order mesoscopic contact angle in the intermediate region that spans (for $0 < \xi < 1$) all length scales between those of the inner region (corresponding to $\xi = 0$) and of the outer region (corresponding to $\xi = 1$). Moreover, that K_0 depends on $S - x$ through the variable ξ defined in equation (3.17) implies that the leading-order mesoscopic contact angle is a slowly varying function of distance from the contact line on all such length scales. It is these observations that motivate the combination of the scaling (3.17) with the change of variable $h = (S - x)K(\xi, T)$ under which it is readily shown that the thin-film equation (2.1) becomes

$$-\lambda^{1-\xi}\frac{\partial K}{\partial T} - \dot{S}\left(K + \epsilon\frac{\partial K}{\partial \xi}\right) + \left(1 + \epsilon\frac{\partial}{\partial \xi}\right)\left(K^3\frac{\partial K}{\partial \xi} - \epsilon^2 K^3\frac{\partial^3 K}{\partial \xi^3}\right)$$
$$+\lambda^{(3-n)\xi}\left(n - 2 + \epsilon\frac{\partial}{\partial \xi}\right)\left(K^3\frac{\partial K}{\partial \xi} - \epsilon^2 K^3\frac{\partial^3 K}{\partial \xi^3}\right) = \mathcal{J}.$$

For $n < 3$, it follows that the differential equation (3.13) may be recovered directly from the thin-film equation (2.1) upon expanding $K \sim K_0(\xi, T)$ as $\lambda \to 0$ with $0 < \xi < 1$. Likewise, the boundary conditions (3.14) and (3.15) may be recovered directly by matching with the leading-order solution in the inner region (as $\xi \to 0^+$) and the outer region (as $\xi \to 1^-$), respectively. This route to the boundary value problem (3.13)–(3.15) for K_0 was taken by [19] for the case in which $\mathcal{J} = 0$ and $n = 2$ (see also [23]) and by [7] for the case in which $n = 2$ and $J \propto T^{-1/2}$ (though [7] does not analyse analytically the functional form of the contact-line law (3.16), a straightforward analysis that we shall report in Section 3.3). That the intermediate problem (3.13)–(3.15) may be derived without proceeding to higher order in the inner region expedites the matched-asymptotic analysis, and we shall therefore make use of intermediate regions with these properties in this paper. The identification of a mesoscopic contact angle satisfying the intermediate problem (3.13)–(3.15) allows us to extract through its analysis valuable physical insight into the effect of uniform mass transfer on the contact-line motion, as we shall now describe.

3.3 Analysis of the contact-line law

In the absence of mass transfer, (3.13)–(3.14) implies $K_0 = (1 + 3\dot{S}_0\xi)^{1/3}$ and hence, by equation (3.15), Tanner's law in the conventional form (see, for example, [39])

$$\dot{S}_0 = \mathcal{V}(\Theta_0, 0) = \frac{1}{3}\left(\Theta_0^3 - 1\right). \tag{3.19}$$

Thus, the contact-line law (3.16) generalises Tanner's law to account for the effects of uniform mass loss ($\mathcal{J} > 0$) or mass gain ($\mathcal{J} < 0$) near the contact line. In this section, we establish the functional form of the contact-line law (3.16) for $\mathcal{J} \neq 0$.

We begin by noting that we require $\Theta_0 > 0$ and $K_0(\xi, t) > 0$ for $0 < \xi < 1$ in order for the film thickness to remain positive at leading order. For $\mathcal{J} \neq 0$ and $\dot{S}_0 \neq 0$, a local

https://doi.org/10.1017/S0956792515000364 Published online by Cambridge University Press

analysis of equation (3.13) implies that

$$\frac{\partial K_0}{\partial \xi} \sim -\frac{\dot{S}_0^4}{\mathcal{J}^3}\left(K_0 + \frac{\mathcal{J}}{\dot{S}_0}\right) \text{ as } K_0 \to -\frac{\mathcal{J}}{\dot{S}_0}.$$

Hence, either $K_0 \equiv -\mathcal{J}/\dot{S}_0$ for $0 \leqslant \xi \leqslant 1$ or $K_0 \neq -\mathcal{J}/\dot{S}_0$ for $0 \leqslant \xi \leqslant 1$. In the first case, the boundary conditions (3.14)–(3.15) imply that $K_0 = 1$ for $0 \leqslant \xi \leqslant 1$, and hence that $\mathcal{V}(1, \mathcal{J}) = -\mathcal{J}$. In the second case, $\partial K_0/\partial \xi$ cannot change sign for $0 \leqslant \xi \leqslant 1$, and we can separate the variables in equation (3.13) and apply equation (3.14) to deduce that $K_0(\xi, T)$ is uniquely determined by

$$\int_1^{K_0} \frac{\eta^3}{\mathcal{J} + \mathcal{V}\eta}\, \mathrm{d}\eta = \xi. \tag{3.20}$$

Evaluating the integral on the left-hand side of equation (3.20) and applying the boundary condition (3.15) implies that $\mathcal{V}(\Theta_0, \mathcal{J})$ is given by the transcendental equation

$$\frac{\Theta_0^3 - 1}{3\mathcal{V}} - \frac{\mathcal{J}(\Theta_0^2 - 1)}{2\mathcal{V}^2} + \frac{\mathcal{J}^2(\Theta_0 - 1)}{\mathcal{V}^3} - \frac{\mathcal{J}^3}{\mathcal{V}^4} \ln\left|\frac{\mathcal{J} + \mathcal{V}\Theta_0}{\mathcal{J} + \mathcal{V}}\right| = 1, \tag{3.21}$$

provided (i) $\Theta_0 \neq 1$, (ii) $\mathcal{V} \neq 0$ and (iii) $-\mathcal{J}/\mathcal{V}$ is not equal to, or between, 1 and Θ_0 (so that K_0 is positive for $0 < \xi < 1$ and we avoid integrating over the non-integrable singularity in the integrand in equation (3.20)). Under conditions (i)–(iii), the integrand in equation (3.20) is either positive (giving $\Theta_0 > 1$) or negative (giving $\Theta_0 < 1$) throughout the range of integration, so that $\mathcal{V}$ is uniquely determined in terms of Θ_0 and $\mathcal{J}$ by the transcendental equation (3.21). Thus, condition (iii) selects the physically relevant root $\mathcal{V}$ of equation (3.21) away from the two special cases in which condition (i) or (ii) is violated. Condition (i) is violated when $\Theta_0 = 1$, in which case the solution is simply given by $K_0 = 1$ for $0 \leqslant \xi \leqslant 1$, so that $\mathcal{V}(1, \mathcal{J}) = -\mathcal{J}$. Condition (ii) is violated when $\mathcal{V} = 0$, in which case the solution is given by $K_0 = (1 + 4\mathcal{J}\xi)^{1/4}$ for $0 \leqslant \xi \leqslant 1$, so that $\mathcal{V}((1 + 4\mathcal{J})^{1/4}, \mathcal{J}) = 0$, provided $\mathcal{J} \geqslant -1/4$. We note that the relationship $\mathcal{V}((1 + 4\mathcal{J})^{1/4}, \mathcal{J}) = 0$ with $\mathcal{J} > 0$ arises in the corresponding slow-time analysis of a pinned contact line in [20].

Having established that $\mathcal{V}$ is uniquely determined in terms of Θ_0 and $\mathcal{J}$, we are now in a position to characterise the contact-line law (3.16). Instead of prescribing $\mathcal{J}$ and Θ_0 and using a root-finding algorithm to determine $\mathcal{V}$ from equation (3.21) subject to the conditions (i)–(iii), we prescribe $\dot{S}_0 = \mathcal{V}$ and solve the initial value problem (3.13)–(3.14) (using *ode15s* in MATLAB with stringent error tolerances) and subsequently read off Θ_0 from the end condition (3.15). We plot some typical results in Figure 2(a), which illustrates that there are two qualitatively distinct classes of contact-line law corresponding to the regimes in which there is mass loss ($\mathcal{J} > 0$) and mass gain ($\mathcal{J} < 0$), the borderline case in which $\mathcal{J} = 0$ corresponding to Tanner's law (3.19). For all $\mathcal{J}$, the plots in Figure 2(a) suggest that the contact-line velocity $\mathcal{V}$ is a continuous increasing function of Θ_0 and a continuous decreasing function of $\mathcal{J}$, facts that may be verified by consideration of elementary properties of the integrand in equation (3.20).

For $\mathcal{J} \leqslant 0$, the contact-line velocity $\mathcal{V}(\Theta_0, \mathcal{J})$ is bounded below by $\mathcal{V}(0, \mathcal{J})$. Since $\mathcal{V}(0, -1/4) = 0$, $\mathcal{V}(0, 0) = -1/3$ and $\mathcal{V}(0, \mathcal{J})$ decreases with $\mathcal{J}$, it follows that $-1/3 < \mathcal{V}(0, \mathcal{J}) < 0$ for $-1/4 < \mathcal{J} < 0$ and $\mathcal{V}(0, \mathcal{J}) > 0$ for $\mathcal{J} < -1/4$, as illustrated in

https://doi.org/10.1017/S0956792515000364 Published online by Cambridge University Press

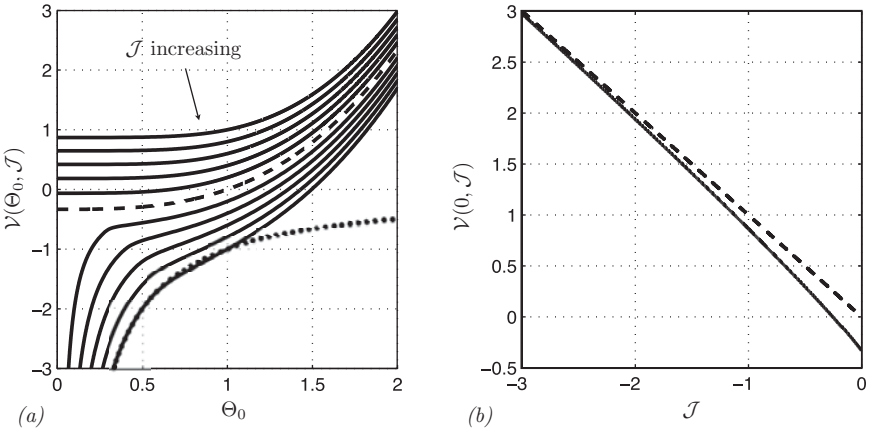

FIGURE 2. (a) Plot of the leading-order contact-line law $\dot{S}_0 = \mathcal{V}(\Theta_0, \mathcal{J})$ (solid lines) for $\mathcal{J} = -1$, $-0.8, \ldots 0.8, 1$ ($\mathcal{J}$ increasing down the page); the dashed line is Tanner's law (3.19) corresponding to $\mathcal{J} = 0$; the dotted line is the asymptote $\dot{S}_0 = -\mathcal{J}/\Theta_0$ for $\mathcal{J} = 1$. (b) Plot of the minimum contact-line velocity $\mathcal{V}(0, \mathcal{J})$ (solid line), which exists for $J \leqslant 0$, and the leading-order term in the asymptote (3.22) (dashed line).

Figure 2(b). Thus, while the contact line can both advance and retreat for $\mathcal{J} \geqslant -1/4$, it can only advance for $\mathcal{J} < -1/4$. A standard asymptotic analysis of equation (3.21) gives

$$\mathcal{V}(\Theta_0, \mathcal{J}) \sim -\mathcal{J} + \mathcal{J}(1 - \Theta_0) \exp\left(\mathcal{J} + \frac{\Theta_0^3 - 1}{3} + \frac{\Theta_0^2 - 1}{2} + \Theta_0 - 1\right), \tag{3.22}$$

as $\mathcal{J} \to -\infty$ for $\Theta_0 \geqslant 0$, so that, in particular, $\mathcal{V}(0, \mathcal{J})$ approaches rapidly its asymptote $-\mathcal{J}$ as $\mathcal{J} \to -\infty$, as illustrated in Figure 2(b). The leading-order term in the asymptote in equation (3.22) follows from the expansion $K_0 \sim 1$ as $\mathcal{J} \to -\infty$ pertaining except in a boundary layer at $\xi = 1$ in which $K_0 \sim K_{00}$ as $\mathcal{J} \to -\infty$ with $\overline{\xi} = |\mathcal{J}|(1 - \xi) = \mathrm{O}(1)$, whereby

$$K_{00}^3 \frac{\partial K_{00}}{\partial \overline{\xi}} = 1 - K_{00} \text{ for } \overline{\xi} > 0; \quad K_{00}(0, T) = \Theta_0, \; K_{00}(\infty, T) = 1, \tag{3.23}$$

a boundary value problem that may readily be solved by separation of variables. The expansion (3.22) and corresponding matched-asymptotic analysis of K_0 hold so long as $1 \ll |\mathcal{J}| \ll 1/\epsilon$, the boundary layer then being much narrower than the outer region in Section 3.1. When $|\mathcal{J}| = \mathrm{O}(1/\epsilon)$, mass gain is of order unity and the relevant distinguished limit is the one considered in Section 4.

For $\mathcal{J} > 0$, the plots in Figure 2(a) suggests that $\mathcal{V}(\Theta_0, \mathcal{J})$ is unbounded below as $\Theta_0 \to 0^+$. This is confirmed by a standard asymptotic analysis of equation (3.21), revealing that

$$\mathcal{V}(\Theta_0, \mathcal{J}) \sim -\frac{\mathcal{J}}{\Theta_0} - \frac{\mathcal{J}(1 - \Theta_0)}{\Theta_0^2} \exp\left(-\frac{\mathcal{J}}{\Theta_0^4} + \frac{1}{3\Theta_0^3} + \frac{1}{2\Theta_0^2} + \frac{1}{\Theta_0} - \frac{11}{6}\right), \tag{3.24}$$

https://doi.org/10.1017/S0956792515000364 Published online by Cambridge University Press

as $\mathcal{J} \to \infty$ or $\Theta_0 \to 0^+$, so that, in particular, $\mathcal{V}$ approaches rapidly its asymptote $-\mathcal{J}/\Theta_0$ as $\Theta_0 \to 0^+$, as illustrated in Figure 2(a) for $\mathcal{J} = 1$. It follows from equation (3.24) that, if a root-finding algorithm were used to determine $\mathcal{V}$ from equation (3.21) as mentioned above, then it would be necessary to address the numerical issues that may arise when the root is exponentially close to a singularity when $\mathcal{J}$ is large or Θ_0 small. The leading-order term in the asymptote in equation (3.24) follows from the expansion $K_0 \sim \Theta_0$ as $\mathcal{J} \to \infty$ or $\Theta_0 \to 0^+$ pertaining except near $\xi = 0$, though the spatial asymptotic structure near $\xi = 0$ is different depending on which limit is taken, as we shall now describe.

If $\Theta_0 = \mathrm{O}(1)$ as $\mathcal{J} \to \infty$, there is a boundary layer at $\xi = 0$ in which $K_0 \sim K_{00}$ as $\mathcal{J} \to \infty$ with $\overline{\xi} = \mathcal{J}\xi = \mathrm{O}(1)$, whereby

$$K_{00}^3 \frac{\partial K_{00}}{\partial \overline{\xi}} = 1 - \frac{K_{00}}{\Theta_0} \text{ for } \overline{\xi} > 0; \quad K_{00}(0, T) = 1,\ K_{00}(\infty, T) = \Theta_0. \tag{3.25}$$

The expansion (3.24) and corresponding matched-asymptotic analysis hold so long as $1 \ll \mathcal{J} \ll 1/\epsilon$, the boundary layer then being much wider than the inner region in Section 3.2. When $\mathcal{J} = \mathrm{O}(1/\epsilon)$, mass loss is of order unity and the relevant distinguished limit is once again the one considered in Section 4.

If $\mathcal{J} = \mathrm{O}(1)$ as $\Theta_0 \to 0^+$, there is a boundary layer at $\xi = 0$ in which $K_0 \sim (1 - 3\mathcal{J}\xi/\Theta_0)^{1/3}$ for $0 < 3\mathcal{J}\xi/\Theta_0 < 1$ (corresponding to a balance between the two terms on the left-hand side of equation (3.14)), an intermediate layer then being required to match the two leading-order solutions via the expansion $K_0 \sim \Theta_0 K_{00}$ with $3\mathcal{J}\xi/\Theta_0 = 1 + 3\Theta_0^3\,\overline{\xi}$, whereby

$$K_{00}^3 \frac{\partial K_{00}}{\partial \overline{\xi}} = 1 - K_{00} \text{ for } \overline{\xi} > 0; \quad K_{00}(\overline{\xi}, T) \sim \left(-3\overline{\xi}\right)^{1/3} \text{ as } \overline{\xi} \to -\infty,\ K_{00}(\infty, T) = 1.$$

The expansion (3.24) and corresponding matched-asymptotic analysis hold so long as $\epsilon \ll \Theta_0 \ll 1$, the boundary layer at $\xi = 0$ then being much wider than the inner region in Section 3.2. As Θ_0 decreases to $\mathrm{O}(\epsilon)$, the leading-order contact-line velocity, $\epsilon\dot{S}_0$, increases to O(1), breaking the dominance of capillarity in both the outer region in Section 3.1 and the inner region in Section 3.2.

Since the leading-order solution $K_0 \sim \Theta_0$ as $\Theta_0 \to 0^+$ or $\mathcal{J} \to \infty$ corresponds to the balance $\partial h/\partial t \sim -\epsilon\mathcal{J}$ holding in the intermediate region except near the contact line, the asymptote $\mathcal{V} \sim -\mathcal{J}/\Theta_0$ represents physically the contact-line motion being dominated by the removal of liquid near the contact line. Thus, as $\Theta_0 \to 0^+$ or $\mathcal{J} \to \infty$, mass loss dominates over capillarity and produces, in particular, the singularity in the contact-line law at $\Theta_0 = 0$ illustrated in Figure 2(b). That such a singularity does not arise as $\Theta_0 \to 0^+$ for $\mathcal{J} < 0$ implies that, loosely speaking, surface tension is able to combat mass gain (see also the discussion in Section 4.2).

The story is much simpler for large Θ_0, for which equation (3.21) implies

$$\mathcal{V} \sim \frac{\Theta_0^3 - 1}{3} - \frac{3\mathcal{J}}{2\Theta_0} \text{ as } \Theta_0 \to \infty, \tag{3.26}$$

so that, for all $\mathcal{J}$, the contact-line law asymptotes to Tanner's law (3.19) at large macroscopic contact angles Θ_0, as indicated in Figure 2(a).

https://doi.org/10.1017/S0956792515000364 Published online by Cambridge University Press

Finally, we note that, while [7] derives an expression equivalent to (3.21) in a small-slip slow-timescale analysis of equations (2.1)–(2.2), with $n = 2$ and $J \propto T^{-1/2}$, and present a numerical analysis pertinent to their particular problem, they do not report an analysis of the contact-line law (3.16) and hence, in particular, the existence of a singularity at $\Theta_0 = 0$ for $\mathcal{J} > 0$. This singularity plays an important role in the evolution of the drop, as we shall describe in Section 5.

3.4 Early-time evolution

At leading order as $\lambda \to 0$, the problem has been reduced to the solution of the pair of nonlinear ordinary differential equations (3.4) and (3.16) for $S_0(T)$ and $\Theta_0(T)$. In order to derive the relevant initial conditions, it is necessary to consider the early time evolution. On the timescale $t = \mathrm{O}(1)$ as $\lambda \to 0$ with $\mathcal{J} = \mathrm{O}(1)$, the spatial asymptotic structure is the same as on the slow timescale $T = \mathrm{O}(1)$ because the contact-line velocity is of $\mathrm{O}(\epsilon)$, though the details in each region are different, as we shall now describe.

Expanding $s \sim 1 + \epsilon s_1$ and $h \sim h_0$ as $\lambda \to 0$, we find that the leading-order outer problem is given by

$$\frac{\partial h_0}{\partial t} + \frac{\partial}{\partial x}\left(h_0^3 \frac{\partial^3 h_0}{\partial x^3}\right) = 0 \text{ for } 0 < x < 1. \tag{3.27}$$

Applying equation (2.2*a, b*) and matching with the intermediate region below gives the boundary conditions

$$\frac{\partial h_0}{\partial x} = 0,\ \frac{\partial^3 h_0}{\partial x^3} = 0 \text{ at } x = 0; \quad h_0 = 0,\ -\frac{\partial h_0}{\partial x} = \theta_0(t) \text{ at } x = 1^-, \tag{3.28}$$

where the leading-order macroscopic contact angle $\theta_0(t)$ is determined as part of the solution to the correctly specified boundary-value problem (3.27)–(3.28) (there being a total of four degrees of freedom in the local expansions of h_0 at $x = 0,\ 1$, namely the film thickness and curvature at $x = 0$ and the contact angle $\theta_0(t)$ and curvature at $x = 1$; we note that the local analysis of equation (3.27) at $x = 1$ also implies that there is no flux of liquid out of the outer region at leading order). As described in [26], for example, equations (3.27)–(3.28) govern the relaxation of the profile under surface tension from its prescribed initial value, $h_0(x, 0) = \mathcal{H}(x)$ for $0 < x < 1$, to the stationary-steady-state profile in which the curvature, and hence the pressure, is constant, so that the large-time attractor is given by

$$h_0(x, t) \to \frac{3M}{2}(1 - x^2),\ \theta_0(t) \to 3M \text{ as } t \to \infty. \tag{3.29}$$

The scalings in the inner and intermediate regions are the same as in Section 3.2, with $\dot{s}_1$, θ_0 and t replacing $\dot{S}_0$, Θ_0 and T, respectively. It follows that the leading-order contribution to the contact-line velocity is determined as part of the leading-order solution in the intermediate region, with equation (3.16) being recovered in the form $\dot{s}_1 = \mathcal{V}(\theta_0, \mathcal{J})$. Since $\theta_0(t)$ is determined as part of the solution to the leading-order outer problem (3.27)–(3.28), $s_1(t)$ is determined by integrating $\dot{s}_1 = \mathcal{V}(\theta_0, \mathcal{J})$ (in practice using quadrature) subject to the initial condition $s_1(0) = 0$. Since $\theta_0(t) \to 3M$ as $t \to \infty$, it follows that $s_1(t) \sim \mathcal{V}(3M, \mathcal{J})t$ as $t \to \infty$. Thus, the expansion for s becomes non-uniform when

https://doi.org/10.1017/S0956792515000364 Published online by Cambridge University Press

$t = \mathrm{O}(1/\epsilon)$ as $\lambda \to 0$ for $3M \neq (1+4\mathcal{J})^{1/4}$; for $3M = (1+4\mathcal{J})^{1/4}$, a non-uniformity must arise at higher order in the expansion of s because the drop begins to lose or gain an order-unity amount of mass on the timescale in which $t = \mathrm{O}(1/\epsilon)$. Finally, we match the fast and slow timescales to deduce that the initial conditions for the coupled nonlinear ordinary differential equations (3.4) and (3.16) for $S_0(T)$ and $\Theta_0(T)$ are given by

$$S_0(0) = 1, \ \Theta_0(0) = 3M. \tag{3.30a,b}$$

In Section 5 we will analyse the resulting evolution of the two-dimensional drop.

4 Small-slip asymptotics with order-unity mass transfer

In this section, we consider the second distinguished limit, namely $J = \mathrm{O}(1)$ as $\lambda \to 0$. The contact-line motion is now on the timescale $t = \mathrm{O}(1)$ and the spatial asymptotic structure consists of two regions: an outer region away from the contact line and an inner region of size of $\mathrm{O}(\lambda)$ at the contact line. In contrast to the asymptotic analysis in the case of small mass transfer in Section 3, for mass transfer of order unity, the leading-order outer and inner solutions may be matched directly, *i.e.* it is not necessary to proceed to higher order in the inner region or to introduce an intermediate region.

4.1 Inner region

We begin with the inner region in which the scalings $x = s + \lambda X$, $h = \lambda H$ are the same as in Section 3.2. Expanding $H \sim H_0$ and $s \sim s_0$ as $\lambda \to 0$, equation (3.7) becomes

$$\left(H_0^3 + H_0^n\right)\frac{\partial^3 H_0}{\partial X^3} = \dot{s}_0 H_0 + J(-X) \text{ for } X < 0. \tag{4.1}$$

Thus, mass transfer is now so strong that it balances the effects of viscous dissipation and capillarity in the inner region. Applying the boundary conditions (2.2*a,b*) and matching with the outer region below results in the boundary conditions (cf. equation (3.8))

$$H_0 = 0, \ -\frac{\partial H_0}{\partial X} = 1 \text{ on } X = 0^-; \quad H_0 \sim \theta_0(-X) \text{ as } X \to -\infty, \tag{4.2a-c}$$

where $\theta_0(t)$ is the leading-order outer macroscopic contact angle. We note that a similar inner problem involving mass loss with $n = 2$ arises in the asymptotic analyses of [2, 7]; however, in both of these papers the corresponding outer balance is different from that in Section 4.2.

We next need to check whether the inner problem (4.1)–(4.2) is correctly specified and in particular whether θ_0 is determined by its solution or must be imposed: as we now show, the former applies when $J < 0$ and the latter when $J > 0$.

https://doi.org/10.1017/S0956792515000364 Published online by Cambridge University Press

At the contact line, the local expansion is given by (*cf.* (2.4))

$$H_0 \sim (-X) + \begin{cases} B_1(-X)^2 + C(-X)^{4-n} & \text{for } n < 2, \\ -\dfrac{(\dot{s}_0 + J)}{2}(-X)^2 \ln(-X) + B_1(-X)^2 & \text{for } n = 2, \\ C(-X)^{4-n} + B_1(-X)^2 & \text{for } 2 < n < 3, \end{cases} \tag{4.3}$$

as $X \to 0^-$, where $B_1(t)$ is the only degree of freedom and $C(t)$ is given by equation (2.5) with $\lambda = 1$ and $\dot{s}_0$ replacing $\dot{s}$. In the far field, equation (4.2*c*) demands that $H_0 \sim \theta_0(-X) + \widehat{H}$, where $\widehat{H} = \mathrm{o}(-X)$ as $X \to -\infty$. Substituting this expansion into equation (4.1) implies that (cf. equation (2.3))

$$\theta_0^3(-X)^3 \frac{\partial^3 \widehat{H}}{\partial X^3} \sim (\dot{s}_0\theta_0 + J)(-X) + \dot{s}_0\widehat{H} \text{ as } X \to -\infty. \tag{4.4}$$

Hence, equation (4.2*c*) is incompatible with equation (4.1) unless

$$\dot{s}_0 = -\frac{J}{\theta_0}. \tag{4.5}$$

We note that this novel contact-line law is consistent with equation (3.22) upon setting $\theta_0 = 1$, as well as with equation (3.24) but with no such restriction on θ_0. This raises a question concerning the self-consistency of the distinguished limits considered here and in Section 3 that we shall resolve shortly.

We proceed with the far-field expansion by using the scaling properties of equation (4.4) subject to equation (4.5) to deduce that the leading term in $\widehat{H}$ is proportional to $(-X)^p$ as $X \to -\infty$, where p is a complex constant and we require that $\mathrm{Re}(p) < 1$ (so that $\widehat{H} = \mathrm{o}(-X)$ as $X \to -\infty$). Substitution gives

$$p(p-1)(p-2) = -\frac{\dot{s}_0}{\theta_0^3} = \frac{J}{\theta_0^4}. \tag{4.6}$$

The cubic equation (4.6) proves crucial in the analysis of both the inner and outer regions: as we now show, for $J > 0$ it has two roots with $\mathrm{Re}(p) < 1$ (admissible in the far field of equation (4.1) but not in the near field as $x \to s_0^-$ of the outer region governed by equation (4.11)) and one with $\mathrm{Re}(p) > 1$ (inadmissible in equation (4.1) but admissible in equation (4.11)); this count reverses for $J < 0$, with important macroscopic consequences in terms of the differences in the respective outer formulations.

To establish the structure of the roots of equation (4.6), it is perhaps simplest to plot the left- and right-hand sides as a function of p, as illustrated in Figure 3(a). The left-hand side of equation (4.6) is zero for $p = 0, 1, 2$, has a local maximum of $2/\sqrt{27}$ at $p = 1 - 1/\sqrt{3}$ and a local minimum of $-2/\sqrt{27}$ at $p = 1 + 1/\sqrt{3}$. Hence, equation (4.6) has three distinct real roots if $|J/\theta_0^4| < 2/\sqrt{27}$, two distinct real roots (one repeated) if $|J/\theta_0^4| = 2/\sqrt{27}$ and one real root and two complex-conjugate roots if $|J/\theta_0^4| > 2/\sqrt{27}$. We plot in Figures 3(b) and (c) the real and imaginary parts of the roots as a function of J/θ_0^4.

https://doi.org/10.1017/S0956792515000364 Published online by Cambridge University Press

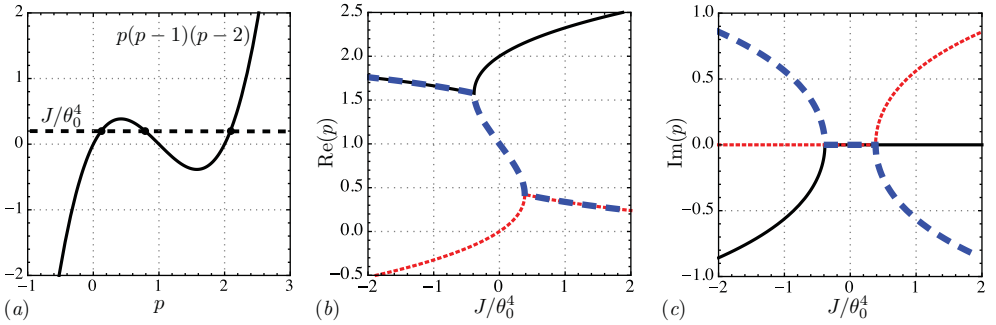

FIGURE 3. (a) Plot of $p(p-1)(p-2)$ (solid line) and J/θ_0^4 (dashed line), with solid circles labelling the three distinct real roots of equation (4.6) that exist for $|J/\theta_0^4| < 2/\sqrt{27}$; see text for details. Plot of (b) the real part and (c) the imaginary part of the roots of the cubic equation (4.6) for p given J/θ_0^4.

For $J > 0$, it follows that the far-field expansion is given by

$$H_0 \sim \theta_0(-X) + \begin{cases} B_2(-X)^{p_1} + B_3(-X)^{p_2} & \text{for } 0 < J/\theta_0^4 < 2/\sqrt{27}, \\ (B_2 \ln(-X) + B_3)(-X)^{p_c} & \text{for } J/\theta_0^4 = 2/\sqrt{27}, \\ B_2(-X)^{p_r} \cos(p_i \ln(-X) + B_3) & \text{for } J/\theta_0^4 > 2/\sqrt{27}, \end{cases} \tag{4.7}$$

as $X \to -\infty$, where $B_2(t)$ and $B_3(t)$ are the only degrees of freedom; p_1 and p_2 are the real roots of equation (4.6) satisfying $0 < p_1 < 1 - 1/\sqrt{3} < p_2 < 1$ for $0 < J/\theta_0^4 < 2/\sqrt{27}$ (corresponding to the red-dotted and blue-dashed curves, respectively, in Figures 3(b) and (c)); $p_c = 1 - 1/\sqrt{3}$ is the double root of (4.6) for $J/\theta_0^4 = 2/\sqrt{27}$ (corresponding to the highest intersection point of the blue-dashed and red-dotted curves in Figure 3(b)); and $p_r \pm \mathrm{i}p_i$ are the complex conjugate roots of equation (4.6) satisfying $0 < p_r < 1 - 1/\sqrt{3}$ for $J/\theta_0^4 > 2/\sqrt{27}$ (corresponding to the blue-dashed and red-dotted curves in Figures 3(b) and (c)). Hence, given $\theta_0(t)$, the order of (4.1) is equal to the total number of degrees of freedom in equations (4.3) and (4.7) (namely, $B_1(t)$, $B_2(t)$, $B_3(t)$), implying that the inner problem (4.1)–(4.2) subject to the contact-line law (4.5) is correctly specified for $J > 0$. The far-field expansions in equation (4.7) reveal the sensitive dependence of the film profile near to the contact line on both θ_0 and J. There is a transition from monotonic behaviour to weak capillary ripples as θ_0 increases through $(\sqrt{27}J/2)^{1/4}$. We note a similar transition in the local analysis of Stokes flow in a wedge driven by evaporation in the diffusion-dominated limit (in which there is a singularity in the evaporative flux at the contact line) is observed by [16].

For $J < 0$, the far-field expansion is given by

$$H_0 \sim \theta_0 (-X) + B_1 (-X)^p \text{ as } X \to -\infty, \tag{4.8}$$

where $B_2(t)$ is the only degree of freedom and p is the negative root of equation (4.6) for $J/\theta_0^4 < 0$ (corresponding to the red-dotted line in Figures 3(b) and (c)). Thus, for $J < 0$, the inner problem (4.1)–(4.2) subject to the contact-line law (4.5) can only be correctly specified if $\theta_0(t)$ is taken to be a degree of freedom belonging to the inner problem. Since

https://doi.org/10.1017/S0956792515000364 Published online by Cambridge University Press

the solution is then given by $H_0 = -X$, it follows that

$$\text{for } J < 0, \quad \theta_0 = 1, \tag{4.9}$$

which fixes both the leading-order macroscopic contact angle (to be equal to the microscopic one) and contact-line velocity, with

$$\text{for } J < 0, \quad \dot{s}_0 = -J, \tag{4.10}$$

reducing thereby the leading-order outer problem from a free-boundary problem to one on a prescribed expanding domain. We note that the novel contact-line law (4.10) is consistent with equation (3.22).

4.2 Outer region

In the outer region we expand $h \sim h_0$ as $\lambda \to 0$ to obtain

$$\frac{\partial h_0}{\partial t} + \frac{\partial}{\partial x}\left(h_0^3 \frac{\partial^3 h_0}{\partial x^3}\right) = -J \text{ for } 0 < x < s_0. \tag{4.11}$$

Applying equation (2.2*a, b*) and matching with the inner region results in the boundary conditions

$$\frac{\partial h_0}{\partial x} = 0, \ \frac{\partial^3 h_0}{\partial x^3} = 0 \text{ at } x = 0; \quad h_0 = 0, \ -\frac{\partial h_0}{\partial x} = \theta_0 \text{ at } x = s_0^-. \tag{4.12$a-d$}$$

In addition, for $J > 0$, we must impose the contact-line law (4.5), while for $J < 0$, we must impose the constraint (4.9) and the contact-line law (4.10).

For $J > 0$, the leading-order macroscopic contact angle $\theta_0(t)$ is not determined as part of the leading-order inner problem, so that our asymptotic analysis can only be self-consistent if equations (4.11)–(4.12) subject to equation (4.5) is correctly specified, with $\theta_0(t)$ determined as part of the solution. In contrast, for $J < 0$, the inner problem imposes the additional constraint (4.9), so that our asymptotic analysis can only be self-consistent if equation (4.11)–(4.12) subject to both equations (4.9) and (4.10) is correctly specified. We shall now verify that this is indeed the case.

We begin with the degree-of-freedom count for the outer problem (4.11)–(4.12) subject to equation (4.5), with $J > 0$. Near the line of symmetry, equations (4.11) and (4.12*a,b*) imply that the pertinent local expansion, namely

$$h_0 \sim A_1 + A_2 x^2 \text{ as } x \to 0, \tag{4.13}$$

contains only two degrees of freedom, namely $A_1(t)$ and $A_2(t)$. Near to the contact line, a local analysis of equation (4.11) subject to equations (4.12*c,d*) and the contact-line law (4.5) implies that the local expansion is given by

$$h_0 \sim \theta_0(s_0 - x) - \frac{\dot{\theta}_0}{2\dot{s}_0}(s_0 - x)^2 + \cdots + A_3(s_0 - x)^p, \tag{4.14}$$

where $\theta_0(t)$ and $A_3(t)$ are the only degrees of freedom and p is the only root of equation

https://doi.org/10.1017/S0956792515000364 Published online by Cambridge University Press

(4.6) for $J/\theta_0^4 > 0$ satisfying the constraint $\mathrm{Re}(p) > 1$ (corresponding to the solid line in Figure 3(b) and in fact satisfying $\mathrm{Re}(p) > 2$); we note that the dots $\cdots$ in equation (4.14) indicate that terms of the form $(s_0 - x)^q$ intrude for all integer q between 3 and $\lfloor p \rfloor - 1$ for $p > 3$, as does a term of the form $(s_0 - x)^p \ln(s_0 - x)$ for integer $p \geqslant 3$. It follows that the order of equation (4.11) is equal to the total number of degrees of freedom in equations (4.13) and (4.14) (namely $A_1(t)$, $A_2(t)$, $A_3(t)$, $\theta_0(t)$). We conclude that equations (4.11)–(4.12), together with the contact-line law (4.5), is correctly specified for $J > 0$, the leading-order macroscopic contact angle $\theta_0(t)$ being determined as part of the solution. The local expansion (4.14) ensures that there is no flux of liquid out of the outer region at leading order. We note that, since $p \sim 2 + J/(2\theta_0^4)$ as $J \to 0^+$ in equation (4.14), there is a non-uniformity in the local expansion of h_0 for $\ln(1/(s_0 - x)) = \mathrm{O}(1/J)$ as $J \to 0^+$; similarly, since $p_1 \sim 1 - J/\theta_0^4$ as $J \to 0^+$ in equation (4.7), there is a non-uniformity in the far-field expansion of H_0 for $\ln(1/(-X)) = \mathrm{O}(1/J)$ as $J \to 0^+$. We resolve these non-uniformities in Section 6.1.1 via a singular perturbation analysis of the limit in which $J \to 0^+$. We reconcile thereby the asymptotic structure of the distinguished limit considered in Section 3 as $\mathcal{J} \to \infty$ with the one considered here as $J \to 0^+$.

We now consider the degree-of-freedom count for the outer problem (4.11)–(4.12) subject to equations (4.9) and (4.10), with $J < 0$. Near the line of symmetry, (4.13) pertains. However, for $J < 0$ and $\theta_0 = 1$, the local expansion at the contact line is given by (cf. equation (4.14))

$$h_0 \sim (s_0 - x) + \begin{cases} A_3(s_0 - x)^{p_1} + A_4(s_0 - x)^{p_2} & \text{for } -2/\sqrt{27} < J < 0, \\ (A_3 \log(s_0 - x) + A_4)(s_0 - x)^{p_c} & \text{for } J = -2/\sqrt{27}, \\ A_3(s_0 - x)^{p_r} \cos(p_i \log(s_0 - x) + A_4) & \text{for } J < -2/\sqrt{27}, \end{cases} \tag{4.15}$$

as $x \to s_0^-$, where $A_3(t)$ and $A_4(t)$ are the only degrees of freedom; p_1 and p_2 are the real roots of equation (4.6) satisfying $1 < p_1 < 1 + 1/\sqrt{3} < p_2 < 2$ for $-2/\sqrt{27} < J < 0$ and $\theta_0 = 1$ (corresponding to the solid and blue-dashed curves, respectively, in Figures 3(b) and (c)); $p_c = 1 + 1/\sqrt{3}$ is the double root of equation (4.6) for $J = -2/\sqrt{27}$ and $\theta_0 = 1$ (corresponding to the lowest intersection point of the solid and blue-dashed curves in Figure 3(b)); and $p_r \pm \mathrm{i}p_i$ are the complex-conjugate roots of equation (4.6) satisfying $p_r > 1 + 1/\sqrt{3}$ for $J < -2/\sqrt{27}$ and $\theta_0 = 1$ (corresponding to the solid and blue-dashed curves in Figures 3(b) and (c)). We conclude that there are a total of four degrees of freedom ($A_1(t)$, $A_2(t)$, $A_3(t)$, $A_4(t)$), so that equations (4.11)–(4.12), together with the constraints (4.9) and (4.10), is correctly specified for $J < 0$. The local expansions (4.15) ensure that there is no flux of liquid out of the outer region at leading order and again reveal the sensitive dependence on J of the film profile near to the contact line: there is a transition from monotonic behaviour to weak capillary ripples as J decreases through $-2/\sqrt{27}$. We note that, since the leading-order version of equation (2.2) is satisfied automatically, the leading-order solution h_0 is in fact uniformly valid throughout the half-contact set $0 < x < s_0(t)$ for $J < 0$, $J = \mathrm{O}(1)$ as $\lambda \to 0$, consistent with the leading-order inner solution being $H_0 = -X$ in this regime. However, since $p_1 \sim 1 - J$ as $J \to 0^-$ in (4.15), there is a non-uniformity in the local expansion of h_0 for $\ln(1/(s_0 - x)) = \mathrm{O}(1/|J|)$ as $J \to 0^-$. We shall resolve this non-uniformity in Section 6.2.1 via a singular perturbation

https://doi.org/10.1017/S0956792515000364 Published online by Cambridge University Press

analysis of the sub-limit in which $J \to 0^-$. We reconcile thereby the asymptotic structure of the distinguished limit considered in Section 3 as $\mathcal{J} \to -\infty$ with the one considered here as $J \to 0^-$.

With regard to the physical interpretation of the contact-line law (4.5) for $J > 0$ and equation (4.10) for $J < 0$, we note that differentiating $h_0(s(t), t) = 0$ and applying equations (4.12*d*) and (4.5) gives

$$\frac{\partial h_0}{\partial t} = -\dot{s}_0 \frac{\partial h_0}{\partial x} = \dot{s}_0 \theta_0 = -J \text{ at } x = s_0^-,$$

the local expansion (4.14) for $J > 0$ and the local expansion (4.15) for $J < 0$ ensuring the existence of $\partial h_0/\partial t(s_0^-, t)$. Thus, at leading order the contact-line motion is driven entirely by the addition or removal of liquid near the contact line. The following comments are intended to give some physical insight into the differences in boundary condition count for $J > 0$ and $J < 0$: when adding liquid, the material equilibrates at $\theta_0 = 1$ as it is deposited at the contact line; in the case of mass loss, the material at the contact line at a given time was in the drop interior at previous times and the out-of-equilibrium contact angle $\theta_0(t)$ is able to adjust itself as the droplet contracts.

In each regime the relevant initial conditions are simply given by

$$h_0(x, 0) = \mathcal{H}(x) \text{ for } 0 < x < s_0(0) = 1, \tag{4.16}$$

there being no need to introduce a temporal boundary layer in order to satisfy at leading order the initial conditions (2.7). For future reference we note that it follows from equations (4.11)–(4.12) that at leading order the condition for global conservation of mass is given by

$$\frac{\mathrm{d}}{\mathrm{d}t}\left(\int_0^{s_0} h_0 \,\mathrm{d}x\right) = -J s_0, \tag{4.17}$$

the existence of the integral in this expression being ensured by the local expansion (4.14) for $J > 0$ and the local expansion (4.15) for $J < 0$. In Section 6 we analyse the evolution of the drop in each regime.

5 Evolution with small mass transfer

We now consider the leading-order evolution of the drop in the distinguished limit considered in Section 3. We begin in Section 5.1 with an analysis of the leading-order outer problem (3.4), (3.16) and (3.30) for $S_0(T)$ and $\Theta_0(T)$. In Section 5.2 we compare our leading-order asymptotic predictions with numerical simulations of the thin-film problem (2.1)–(2.2) with $n = 1$ and $\lambda \ll 1$.

5.1 Analysis of the leading-order problem

5.1.1 *Evolution without mass transfer*

In order to put in context the effect of mass transfer on the evolution of the drop, we begin with a brief review of the borderline case in which mass transfer is absent, a case that has been analysed by, amongst others, [19, 26]. In the absence of mass transfer, the

https://doi.org/10.1017/S0956792515000364 Published online by Cambridge University Press

expression (3.4) representing global conservation of mass may be integrated subject to the initial conditions (3.30) to obtain $\Theta_0 S_0^2 = 3M$. Since the contact-line law (3.16) reduces to Tanner's law in the form (3.19) when $\mathcal{J} = 0$, it follows that $S_0(T)$ is governed by the single nonlinear ordinary differential equation

$$\dot{S}_0 = \frac{1}{3}\left(\frac{(3M)^3}{S_0^6} - 1\right), \tag{5.1}$$

with $S_0(T) \equiv 1$. Thus, $S_0 \to (3M)^{1/2}$ and $\Theta_0 \to 1$ as $T \to \infty$, with $S_0(T) \equiv 1$ for $M = 1/3$ (consistent with the solution on the fast timescale in Section 3.4). We plot in Figure 5(a) Tanner's law and some typical trajectories, illustrating the relaxation of the drop back to its equilibrium configuration for comparison below with similar plots for $\mathcal{J} \neq 0$.

5.1.2 *Regime diagram for evolution with mass transfer*

For $\mathcal{J} \neq 0$, we write the conservation-of-mass condition (3.4) in the form

$$\dot{\Theta}_0 = -\frac{3\mathcal{J} + 2\Theta_0 \dot{S}_0}{S_0}, \tag{5.2}$$

to deduce that at any point of intersection of the curve $\dot{S}_0 = -3\mathcal{J}/2\Theta_0$ and the contact-line law $\dot{S}_0 = \mathcal{V}(\Theta_0, \mathcal{J})$ in the $(\Theta_0, \dot{S}_0)$-plane there is a solution in which Θ_0, and hence $\dot{S}_0$, is constant. To establish the existence of such a solution, we substitute $\mathcal{V} = -3\mathcal{J}/2\Theta_0$ into the implicit expression (3.21) for the contact-line velocity $\mathcal{V}$ to obtain the expression

$$\mathcal{J} = F(\Theta_0) \equiv \frac{2\Theta_0}{81}\left(3(1-\Theta_0)(3+6\Theta_0+10\Theta_0^2) + 8\Theta_0^3 \ln\left|2 - \frac{3}{\Theta_0}\right|\right), \tag{5.3}$$

any roots of which must satisfy the conditions (i)–(iii) stated after equation (3.21) in order to be physically relevant. With $-\mathcal{J}/\mathcal{V} = 2\Theta_0/3$, condition (iii) demands that any roots of equation (5.3) satisfy $0 < \Theta_0 < 3/2$. We plot the curve (5.3) in the $(\mathcal{J}, \Theta_0)$-plane in Figure 4(a) for $0 < \Theta_0 < 3/2$ and note that $F(\Theta_0)$ has a maximum at $\Theta_c \approx 0.71517$, with $\mathcal{J}_c = F(\Theta_c) \approx 0.22781$, and is unbounded below as $\Theta_0 \to 3/2^-$. As illustrated in Figure 4(a), we denote by $\Theta_0 = \Theta_-(\mathcal{J})$ the root of (5.3) satisfying $0 < \Theta_0 \leqslant \Theta_c$ for $0 < \mathcal{J} \leqslant \mathcal{J}_c$ and by $\Theta_0 = \Theta_+(\mathcal{J})$ the root satisfying $\Theta_c < \Theta_0 < 3/2$ for $\mathcal{J} < \mathcal{J}_c$.

Since $\dot{\Theta}_0$ is negative for sufficiently large Θ_0 (by (3.26) and (5.2)) and can only vanish when $\Theta_0 = \Theta_-(\mathcal{J})$ for $0 < \mathcal{J} \leqslant \mathcal{J}_c$ or $\Theta_0 = \Theta_+(\mathcal{J})$ for $\mathcal{J} < \mathcal{J}_c$, we deduce that $\dot{\Theta}_0 < 0$ ($\dot{\Theta}_0 > 0$) in the open shaded (unshaded) region of the $(\mathcal{J}, \Theta_0)$-plane shown in Figure 4(a). Combining this result with the fact that the cross-sectional area of the drop decreases (increases) with time for $\mathcal{J} > 0$ ($\mathcal{J} < 0$), we deduce that the evolution of the drop is different in each of the three regimes I, II and III illustrated by the open shaded regions of the $(\mathcal{J}, M)$-plane shown in Figure 4(b), as we shall now describe qualitatively. In regime I both the cross-sectional area and macroscopic contact angle decrease with time. In regime II the cross-sectional area decreases with time, while the macroscopic contact angle may increase or decrease with time depending on whether Θ_0 is less than or greater than $\Theta_+(\mathcal{J})$, respectively. In regime III the cross-sectional area increases with time, while the macroscopic contact angle may increase or decrease with time, once again depending

https://doi.org/10.1017/S0956792515000364 Published online by Cambridge University Press

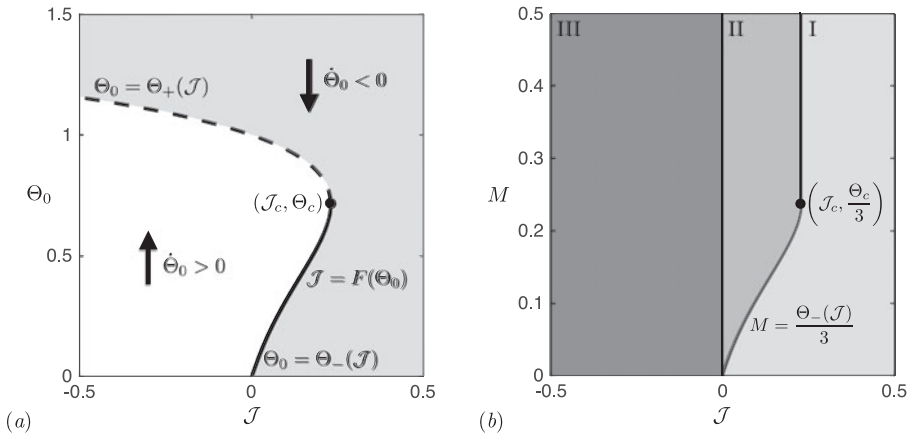

FIGURE 4. (a) The dashed and solid lines form the curve (5.3) for $0 < \Theta_0 < 3/2$; the dashed line is the root $\Theta_0 = \Theta_-(\mathcal{J})$; the solid line is the root $\Theta_0 = \Theta_+(\mathcal{J})$; $\dot{\Theta}_0 < 0$ ($\dot{\Theta}_0 > 0$) in the shaded (unshaded) region. (b) Regime diagram showing the regions corresponding to regimes I, II and III. See text for details.

on whether Θ_0 is less than or greater than $\Theta_+(\mathcal{J})$, respectively. In regimes I and II the solution pertains only up until the time, T_c say, at which the cross-sectional area of the drop vanishes, the extinction time then being given by $t_c \sim T_c/\epsilon$ as $\lambda \to 0$; we note that T_c depends only on $\mathcal{J}$ and M. In regime III the evolution continues for all time, the cross-sectional area of the drop growing without bound as $T \to \infty$.

Before describing quantitatively the dynamics in each regime in Sections 5.1.3–5.1.5, we note that in our numerical simulations we use the following algorithm in MATLAB. At each time step, we use *ode15s* and *fzero* to shoot for $\dot{S}_0 = \mathcal{V}(\Theta_0, \mathcal{J})$ using the current value of Θ_0, except that we use the asymptote (3.24) for small Θ_0 and $\mathcal{J} > 0$ as soon as the relative error between the numerical and asymptotic predictions is smaller than a threshold value (we used 10^{-12}); we then use equation (5.2) to read off the current value of $\dot{\Theta}_0$ given the current values of S_0, Θ_0 and $\dot{S}_0$; finally we step forward in time using *ode15s*. We checked that there is no visible change to our plots when the error tolerances are reduced and we took absolute and relative errors of 10^{-8} or smaller.

5.1.3 *Evolution in regime I*

In this regime either $\mathcal{J} > \mathcal{J}_c$ or $0 < \mathcal{J} \leqslant \mathcal{J}_c$ and $\Theta_0(0) = 3M < \Theta_-(\mathcal{J})$, as illustrated in Figure 4(b). The macroscopic contact angle always decreases with time, as illustrated by the arrows in the shaded region in Figure 4(a) and on the contact-line laws plotted in Figures 5(b)(*i*)–(c)(*i*) for $\mathcal{J} = 0.5$ and $\mathcal{J} = 0.1$, respectively. As illustrated in Figure 5(b)(*ii*)–(*iii*) and (c)(*ii*)–(*iii*), our numerical simulations of equations (3.4) and (3.16) suggest that $\Theta_0(T) \to 0$ and $S_0(T) \to 0$ as $T \to T_c^-$. An asymptotic analysis consistent with these observations using equations (3.4) and (3.24) gives

$$S_0(T) \sim A(T_c - T)^{1/2}, \ \Theta_0(T) \sim \frac{2\mathcal{J}}{A}(T_c - T)^{1/2} \text{ as } T \to T_c^-,$$

https://doi.org/10.1017/S0956792515000364 Published online by Cambridge University Press

where the positive constants A and T_c are determined globally, rather than locally. Our numerical simulations confirm this square-root scaling behaviour near extinction, as illustrated by the plots of $\Theta_0(T)$ and $S_0(T)$ in Figures 6(a) and (b) in which $\Theta_0(0) = 3M$ is slightly smaller than $\Theta_-(\mathcal{J})$ and $\mathcal{J} = 0.1$.

We plot in Figure 6(e) the computed extinction time on the slow timescale, T_c, for $0 < \mathcal{J} < 1$ and for $\Theta_0(0) = 3M = 0.2, 0.4, \ldots, 1.8, 2.0$. As expected, T_c increases with M and decreases with $\mathcal{J}$. We note that there is a very small change in the curvature of the lines in Figure 6(e) when passing through the borderline between regimes I and II.

For large $\mathcal{J}$, we use the leading term in equation (3.24), *i.e.* the asymptote $\dot{S}_0 \sim -\mathcal{J}/\Theta_0$ as $\mathcal{J} \to \infty$, together with the differential equation (3.4) and the initial conditions (3.30), to deduce that

$$S_0 \sim \left(1 - \frac{T}{T_c}\right)^{1/2}, \quad \Theta_0 \sim 3M \left(1 - \frac{T}{T_c}\right)^{1/2}, \quad T_c \sim \frac{3M}{2\mathcal{J}} \text{ as } \mathcal{J} \to \infty. \tag{5.4}$$

That $\dot{S}_0 + \mathcal{J}/\Theta_0$ is exponentially small as $\mathcal{J} \to \infty$ or $\Theta_0 \to 0^+$ by equation (3.24) is consistent with the excellent agreement of the leading-order prediction for T_c in equation (5.4) with our numerical simulations, even for moderate values of $\mathcal{J}$, as illustrated in Figure 6(f).

5.1.4 *Evolution in regime II*

In this regime $0 < \mathcal{J} < \mathcal{J}_c$ and $\Theta_0(0) = 3M > \Theta_-(\mathcal{J})$, as illustrated in Figure 4(b), with $\dot{\Theta}_0 > 0$ for $\Theta_-(\mathcal{J}) < \Theta_0 < \Theta_+(\mathcal{J})$, $\dot{\Theta}_0 = 0$ for $\Theta_0 = \Theta_+(\mathcal{J})$ and $\dot{\Theta}_0 < 0$ for $\Theta_0 > \Theta_+(\mathcal{J})$, as illustrated by the arrows in Figure 4(a) and on the contact-line law plotted in Figure 5(c)(*i*) for $\mathcal{J} = 0.1$. It follows that the macroscopic contact angle is always driven toward $\Theta_+(\mathcal{J})$. Our numerical simulations suggest that for all $\Theta_0(0) = 3M > \Theta_-(\mathcal{J})$, $\Theta_0(T) \to \Theta_+(\mathcal{J})$ as $T \to T_c^-$, as illustrated in Figure 5(c)(*ii*)–(*iii*). A standard asymptotic analysis of (5.2) consistent with this observation gives

$$S_0 \sim \frac{3\mathcal{J}}{2\Theta_+(\mathcal{J})}(T_c - T) \quad \text{as} \quad T \to T_c^-.$$

Our numerical simulations confirm the linear scaling behaviour in the width and thickness of the drop near extinction. For example, the plots of $\Theta_0(T)$ and $S_0(T)$ in Figures 6(c) and (d) show that, for $\Theta_0(0) = 3M$ slightly larger than $\Theta_-(\mathcal{J})$ and $\mathcal{J} = 0.1$, the macroscopic contact angle rapidly approaches $\Theta_+(\mathcal{J})$ and the half-drop width scales linearly with the time until extinction in a small window just before the drop vanishes.

For small $\mathcal{J}$ there are two distinct timescales. On the slow timescale in which $T = \mathrm{O}(1)$ as $\mathcal{J} \to 0^+$, mass loss is absent at leading order and the drop spreads at leading order according to the drop spreading model in Section 5.1.1. Mass loss sets in on the slow-slow timescale in which $\overline{T} = \mathcal{J}T = \mathrm{O}(1)$ as $\mathcal{J} \to 0^+$. Expanding $\Theta_0 \sim \Theta_{00}(\overline{T})$ and $S_0 \sim S_{00}(\overline{T})$ as $\mathcal{J} \to 0^+$, the contact-line law (3.16) gives $\Theta_{00}(\overline{T}) = 1$, the macroscopic contact angle equilibrating on the slow-slow timescale, and thence from equation (3.4) that $S_{00} = 3(\overline{T}_c - \overline{T})/2$, where $\overline{T}_c$ is the leading-order extinction time on the slow-slow timescale. Matching the slow and slow-slow timescales gives the initial condition

https://doi.org/10.1017/S0956792515000364 Published online by Cambridge University Press

$S_{00}(0) = (3M)^{1/2}$, and we deduce that the extinction time on the slow timescale has the expansion

$$T_c \sim \frac{\overline{T}_c}{\mathcal{J}} = \frac{2(3M)^{1/2}}{3\mathcal{J}} \text{ as } \mathcal{J} \to 0^+,$$

which is in excellent agreement with our numerical simulations, as illustrated in Figure 6(g).

5.1.5 *Evolution in regime III*

In this regime $\mathcal{J} < 0$, as illustrated in Figure 4(b), with $\dot{\Theta}_0 > 0$ for $\Theta_0 < \Theta_+(\mathcal{J})$, $\dot{\Theta}_0 = 0$ for $\Theta_0 = \Theta_+(\mathcal{J})$ and $\dot{\Theta}_0 < 0$ for $\Theta_0 > \Theta_+(\mathcal{J})$, as illustrated by the arrows in Figure 4(a) and on the contact-line law plotted in Figure 5(d)(*i*) for $\mathcal{J} = -0.1$. Since the solution continues indefinitely, the drop growing in size for all T, it follows that $\Theta_0(T) \to \Theta_+(\mathcal{J})$ as $T \to \infty$, equation (5.2) then giving

$$S_0 \sim -\frac{3\mathcal{J}T}{2\Theta_+(\mathcal{J})} \text{ as } T \to \infty.$$

Hence, the drop grows at large times with constant macroscopic contact angle $\Theta_+(\mathcal{J}) \in (1, 3/2)$ and with constant contact-line velocity $-3\mathcal{J}/(2\Theta_+(\mathcal{J})) > 0$. We note that $\Theta_+(\mathcal{J}) \to 1$ and $\dot{S}_0 \sim -3\mathcal{J}/2$ as $\mathcal{J} \to 0^-$, while $\Theta_+(\mathcal{J}) \to 3/2$ and $\dot{S}_0 \sim -\mathcal{J}$ as $\mathcal{J} \to -\infty$, the limiting contact-line velocity for large mass gain being set by the rate at which liquid is supplied near the contact line.

The long-time linear scaling behaviour of the drop profile is consistent with our numerical simulations of equations (3.4) and (3.16), *e.g.* some typical trajectories for $\mathcal{J} = -0.1$ are plotted in Figures 5(d)(*ii*)–(*iii*). We note that our numerical simulations are also consistent with the analytical results derived in Section 3.3 that the drop contracts initially before spreading for $-1/4 < \mathcal{J} < 0$ and $\Theta_0(0) = 3M < (1 + 4\mathcal{J})^{1/4}$, but spreads throughout its evolution for $\mathcal{J} < -1/4$.

For small $\mathcal{J} < 0$ there are two distinct timescales as in regime II. The evolution is exactly the same as in regime II on the slow timescale in which $T = \mathrm{O}(1)$ as $\mathcal{J} \to 0^-$, mass gain being absent at leading order during the early relaxation of the drop to its equilibrium position without mass transfer. Mass gain sets in on the slow-slow timescale in which $\overline{T} = |\mathcal{J}|T = \mathrm{O}(1)$ as $\mathcal{J} \to 0^-$, with an analysis similar to that for regime II giving $\Theta_0 \sim 1$ and $S_0 \sim 1 + 3\overline{T}/2$ as $\mathcal{J} \to 0^-$.

For large $\mathcal{J} < 0$, we use equation (3.22) in the form of the asymptote $\dot{S}_0 \sim -\mathcal{J}$ as $\mathcal{J} \to -\infty$, together with the differential equation (3.4) and the initial conditions (3.30), to deduce that the evolution is on the fast timescale in which $\overline{T} = |\mathcal{J}|T = \mathrm{O}(1)$, with

$$S_0 \sim 1 + \overline{T}, \ \Theta_0 \sim \frac{3}{2}\left(1 + \frac{2M-1}{(1+\overline{T})^2}\right) \text{ as } \mathcal{J} \to -\infty; \tag{5.5}$$

we note that the macroscopic contact angle $\Theta_0 \to 3/2$ as $\overline{T} \to \infty$.

https://doi.org/10.1017/S0956792515000364 Published online by Cambridge University Press

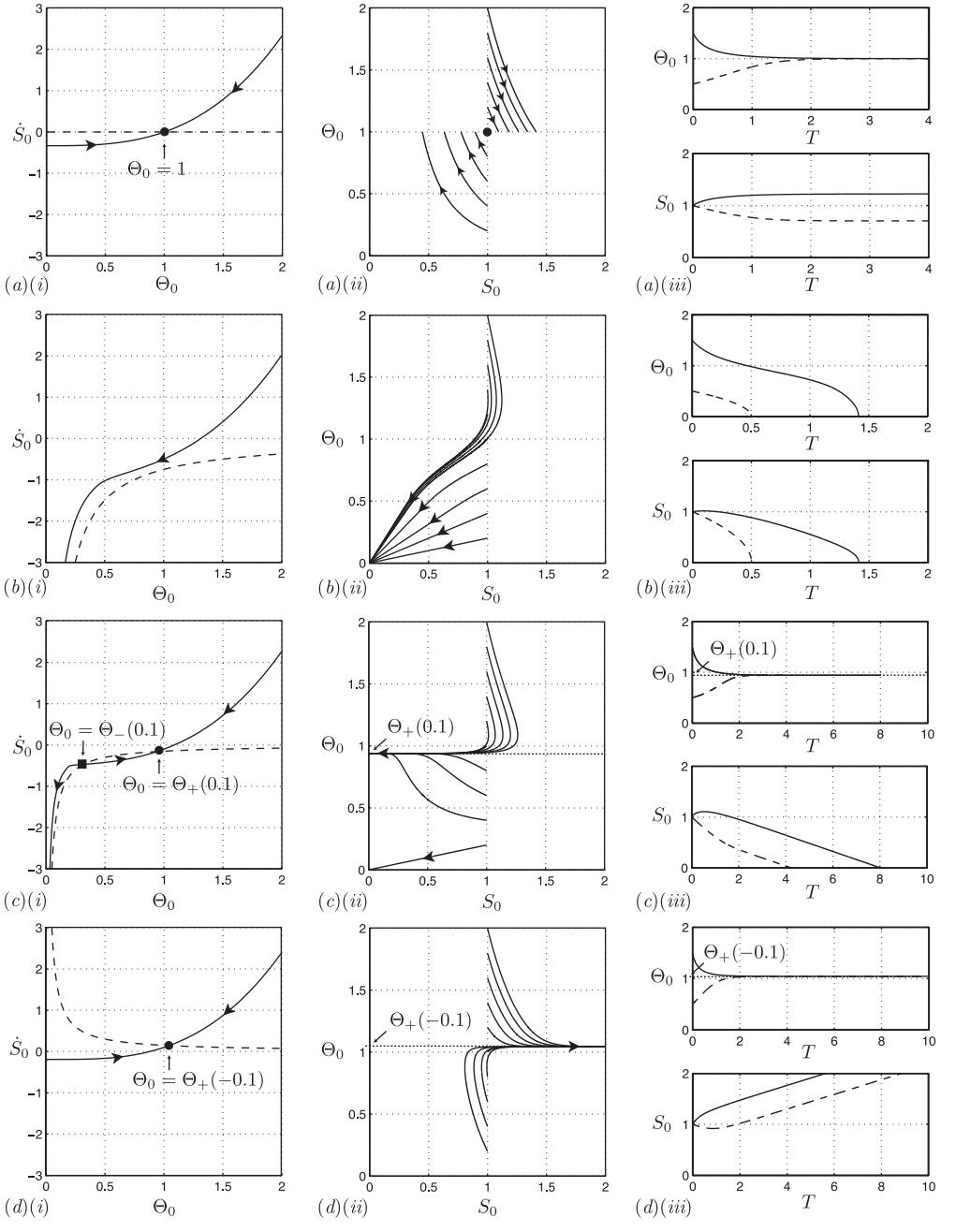

FIGURE 5. Plots for (a) $\mathcal{J} = 0$, (b) $\mathcal{J} = 0.5$, (c) $\mathcal{J} = 0.1$ and (d) $\mathcal{J} = -0.1$. The first column contains plots of the contact-line law and the curve $\dot{S}_0 = -3\mathcal{J}/2\Theta_0$ (dashed line) in the $(\Theta_0, \dot{S}_0)$-plane. The second column contains plots of the (S_0, Θ_0)-phase plane showing the trajectories beginning at $\Theta_0(0) = 3M = 0.2, 0.4, \ldots, 1.8, 2.0$, with $S_0(0) = 1$. The third column contains plots of $\Theta_0(T)$ and $S_0(T)$ for $\Theta_0(0) = 1.5$ (solid line) and $\Theta_0(0) = 0.5$ (dashed line), with $S_0(0) = 1$. In the first and second columns, the arrows indicate the direction of motion as T increases. Note that $\Theta_+(0.1) \approx 0.94002$, $\Theta_+(-0.1) \approx 1.04387$ and $\Theta_-(0.1) \approx 0.32013$. See text for details.

https://doi.org/10.1017/S0956792515000364 Published online by Cambridge University Press

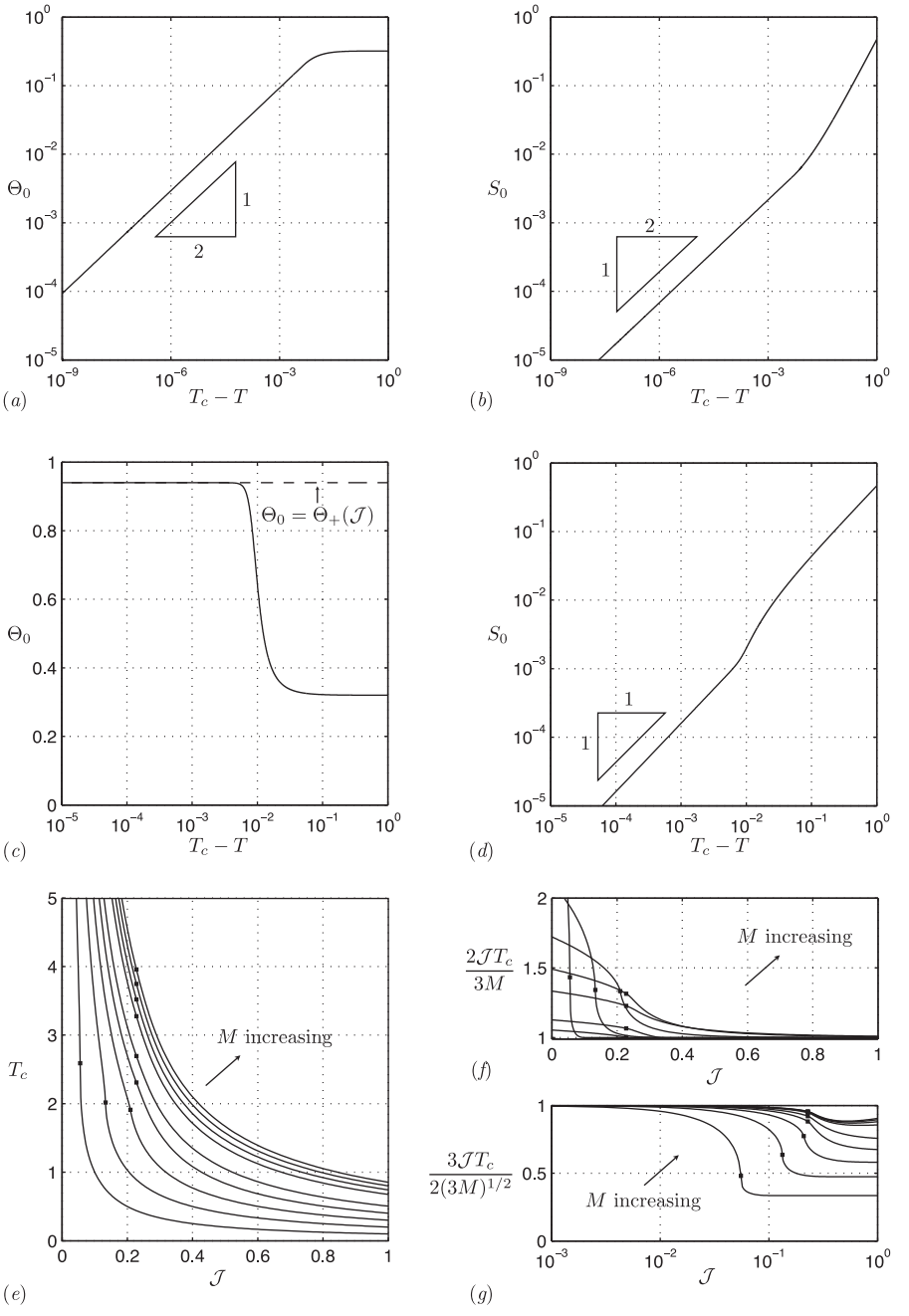

FIGURE 6. Plots of (a) $\Theta_0(T)$ and (b) $S_0(T)$ for $\Theta_0(0) = 3M = 0.32012 < \Theta_-(0.1) \approx 0.32013$, with $S_0(0) = 1$ and $\mathcal{J} = 0.1$; note that $\Theta_0(T) \to 0$ as $T \to T_c^-$, where the extinction time $T_c \approx 2.12821$. Plots of (c) $\Theta_0(T)$ and (d) $S_0(T)$ for $\Theta_0(0) = 3M = 0.32014 > \Theta_-(0.1) \approx 0.32013$, with $S_0(0) = 1$ and $\mathcal{J} = 0.1$; note that $\Theta_0(T) \to \Theta_+(0.1) \approx 0.94002$ as $T \to T_c^-$, where the extinction time $T_c \approx 2.14107$. Plots of (e) T_c, (*f*) $3\mathcal{J}T_c/(2(3M)^{1/2})$ and (g) $2\mathcal{J}T_c/(3M)$ for $\Theta_0(0) = 3M = 0.2, 0.4, \ldots, 1.8, 2.0$ and $0 < \mathcal{J} < 1$; for each value of M, we computed T_c for 370 values of $\mathcal{J}$ carefully distributed over the interval $(0, 1)$; on each line the square indicates the borderline between regimes I and II, with regime I above and regime II below. See text for details.

https://doi.org/10.1017/S0956792515000364 Published online by Cambridge University Press

5.2 Numerical simulations

5.2.1 *Description of the numerical scheme*

We begin by mapping the contact set $0 < x < s(t)$ to a fixed computational domain $0 < \xi < 1$ by setting $x = s(t)\xi$. We then write the resulting version of the thin-film equation (2.1) as a system of two second-order partial differential equations by setting $h(x,t) = \eta(\xi,t)/s(t)$, $p(x,t) = P(\xi,t)/s(t)^3$ to obtain

$$\frac{\partial \eta}{\partial t} - \frac{\partial}{\partial \xi}\left[\left(\frac{\eta^3}{s^7} + \frac{\lambda^{3-n}\eta^n}{s^{4+n}}\right)\frac{\partial P}{\partial \xi} + \frac{\dot{s}\xi\eta}{s}\right] = -Js, \quad \frac{\partial^2 \eta}{\partial \xi^2} = -P \text{ for } 0 < \xi < 1. \tag{5.6}$$

The boundary conditions (2.2) give

$$\frac{\partial \eta}{\partial \xi} = 0, \quad \frac{\partial P}{\partial \xi} = 0 \text{ at } \xi = 0; \quad \eta = 0, \quad -\frac{\partial \eta}{\partial \xi} = -s^2 \text{ at } \xi = 1^-, \tag{5.7}$$

while the moving-boundary condition (2.6) becomes

$$\dot{s} = -J - \frac{\lambda^{3-n}\eta^{n-1}}{s^{3+n}}\frac{\partial P}{\partial \xi} \text{ at } \xi = 1^-. \tag{5.8}$$

As noted in Section 2, at the contact line the pressure gradient is zero for $n < 1$, finite for $n = 1$ and unbounded for $1 < n < 3$. In order to avoid the numerical issues that may arise when there is a removable singularity in the moving-boundary condition (5.8), we take $n = 1$ in our numerical simulations. We emphasise that in both of the distinguished limits considered in Sections 3–4, the leading-order outer formulations are independent of n.

In our numeral simulations we attempted first to implement a finite-difference scheme using the method described by [42], having eliminated P from equations (5.6)–(5.8). The spatial discretisation uses second-order accurate finite differences on a uniform mesh. The resulting system of nonlinear ordinary differential equations for the drop thickness at the spatial mesh points and for $s(t)$ is integrated using *ode15s* in MATLAB, with the Jacobian being evaluated using complex-step differentiation as described in [37]. That the spatial mesh is uniform implies that a large number of grid points is required to resolve the inner regions described in Sections 3–4. For example, demanding there to be 100 grid points within a distance of λ of $\xi = 1$ would require of the order of $100/\lambda$ grid points in total. For $\lambda = 10^{-3}$ and 10^5 grid points, the scheme converges rapidly for $s(t) \gtrapprox 0.1$, but fails to converge in reasonable time for smaller values of $s(t)$.

In order to compute the evolution for smaller values of λ, we concluded that it would be necessary to use a non-uniform spatial grid. It is for this reason that we chose to use an implicit-in-time finite-element method to discretise the partial differential equations (5.6) with $n = 1$ subject to the boundary conditions (5.7); see, for example, [14]. Our finite-element solution uses a linear approximation to the solution on each element and a non-uniform spatial mesh with a high concentration of nodes in a neighbourhood of $\xi = 1$ in order to obtain sufficient spatial resolution of the inner regions described in Sections 3–4. We use an implicit approximation to the time derivative in the moving-boundary condition (5.8) with $n = 1$. On each time step our discretisations are fully coupled and we

https://doi.org/10.1017/S0956792515000364 Published online by Cambridge University Press

use Newton's method to solve the resulting system of nonlinear algebraic equations. We check that our simulations have converged in the usual way by refining the spatial mesh and shortening the time step. We note that, when they both converge, our finite-difference and finite-element schemes are in excellent agreement.

In our numerical simulations, we impose the candidate initial conditions

$$h(x,0) = \mathcal{H}(x) = A(1-x^2) + B(1-x^4) \text{ for } 0 < x < s(0) = 1, \tag{5.9}$$

where the constants $A = 3(5M-1)/4$ and $B = 5(1-3M)/8$ for $M > 1/15$ are chosen so that $\mathcal{H}(x) > 0$ for $0 \leqslant x < 1$ and

$$\int_0^1 \mathcal{H}(x)\,\mathrm{d}x = M,\ \mathcal{H}'(1) = -1, \tag{5.10}$$

where, here and hereafter, a prime $'$ denotes the derivative with respect to the argument. We note that the rate of change of the curvature of the initial profile (at leading order in the thin-film limit), namely $\mathcal{H}'''(x) = -45(M-1/3)x$, varies substantially even for moderate values of $M-1/3$, i.e. away from the special case in which the initial profile is a parabola.

In the case of small mass transfer our asymptotic analysis is based on a small parameter, namely $\epsilon = 1/\ln(1/\lambda)$, that depends logarithmically on λ, so the correction terms not captured by the above analysis will be only logarithmically smaller than those we have derived. Moreover, in this case the leading-order predictions are unchanged upon replacing λ by any order-unity multiple of itself, so it would be necessary to proceed to second-order in the asymptotic analysis if an attempt were to be made to fit λ by comparing the asymptotic predictions with experimental data, as described in [21] for a closely related spreading problem without mass transfer. Since it is in this context that it would be best to undertake an error analysis to ascertain the accuracy of our asymptotic predictions as $\lambda \to 0$, our aims in this paper are much less ambitious. We shall present evidence for the validity of the leading-order asymptotic analyses in Sections 3 and 4 by comparing their predictions with our preliminary numerical simulations, and extract thereby the physical insight afforded by the leading-order analysis with some confidence that it describes the main features of the flow. In this sense our results extend previous analyses in the absence of mass transfer, which have demonstrated the utility of the leading-order analysis; see, for example, [29, 30] and references therein. In our preliminary numerical simulations (presented in Sections 5.2.2, 6.1.5 and 6.2.4), we use the values $M = 1$ or $M = 1/3$ and a value of λ that is toward the lower bound of what may be expected physically, namely $\lambda = 10^{-5}$, so that $\epsilon = 1/\ln(1/\lambda) \approx 0.087$ (except in Section 6.2.4 for reasons given there). We emphasise that an important direction for future research may be to ascertain the accuracy of our asymptotic predictions for $\lambda \gtrsim 10^{-5}$ with a variety of values of M. However, in doing this, the above caveat concerning the importance of the second-order analysis should be borne in mind.

https://doi.org/10.1017/S0956792515000364 Published online by Cambridge University Press

5.2.2 *Comparison of asymptotic and numerical predictions*

In Figures 7(a)–(d) we plot the numerical and leading-order asymptotic solutions for $s(t)$, $m(t)$ and $h(x,t)$ in the four cases corresponding to an absence of mass transfer ($\mathcal{J}=0$), regime I ($\mathcal{J}=0.5$), regime II ($\Theta_0(0)=3M>\Theta_-(\mathcal{J})$, $\mathcal{J}=0.1$) and regime III ($\mathcal{J}=-0.1$). In all of these cases the numerical and asymptotic predictions are in excellent visual agreement, providing quality control for the validity of the small-slip asymptotics in Section 3. It is notable that, as illustrated in Figures 7(a)–(d), in each regime the rapid surface-tension-driven relaxation of the initial profile causes the drop profile at time $t=1$ to be visually indistinguishable from that of the parabolic profile predicted by the leading-order outer solution (3.2). This is despite the rate of change of the curvature of the initial profile, $\mathcal{H}'''(x)=-30x$, being moderately large for $M=1$.

We plot in Figure 8(a) the numerical and leading-order asymptotic predictions of the extinction time for $M=1$ and various values of $\mathcal{J}>0$, revealing excellent visual agreement for those values plotted. However, for the value $\mathcal{J}=0.4$, the extinction time is not plotted in Figure 8(a) because positivity is lost before extinction occurs, as we shall now describe. (We shall discuss shortly the range of intermediate values of $\mathcal{J}$ for which this unexpected phenomenon occurs.) As illustrated in Figure 8(b), for $\mathcal{J}=0.4$, our numerical simulations predict that the drop profile develops a local minimum in the interior of the contact set near to the contact line, forming thereby a small rim of liquid whose extent and thickness are both much larger than the slip length, but much smaller than the outer length scale. The rim proceeds to shrink, the local minimum at $x=x_m(t)$ moving downward and inward before rapidly touching down at an interior point $x=x_m(t_r)$ near to the contact line at time $t=t_r$. Our numerical simulations fail to converge when positivity is lost. Nevertheless, we find through careful refinement of the spatial and temporal meshes that both the horizontal and vertical distances of the interior minimum from the point of touchdown on the substrate scale linearly with the time until touchdown over at least three decades near to touchdown, as illustrated in Figures 8(c)–(d). As touchdown is approached, Figure 8(e) suggests that the pressure at the interior minimum tends to a constant, consistent with the dense clustering of the appropriately scaled free-surface profiles in Figure 8(f), which suggest that in the neighbourhood of the interior minimum the free surface is approximately a parabola of constant curvature, moving with constant velocity downward and inward, at least during a window of time before touchdown. We note that the free-surface profiles begin to deviate from this configuration in the very final stages before touchdown, perhaps due to slip becoming important (the film thickness becoming comparable to the slip length sufficiently near to touchdown) or perhaps because our numerical scheme is losing accuracy (despite our careful refinement of the spatial and temporal meshes).

We emphasise that touchdown occurs outside of the region of validity of the small-slip asymptotics in Section 3 because the half-drop width and mass at touchdown are of order ϵ and ϵ^3, respectively (taking the values $s(t_r)\approx 0.122285$ and $m(t_r)\approx 1.09186\times 10^{-3}$), which would require $\Theta_0(t_r)$ to be of order ϵ. We do not pursue further in this paper this unexpected touchdown phenomenon for which we do not have a convincing explanation, but remark that our numerical simulations suggest that, with $\lambda=10^{-5}$ and the initial conditions given above, touchdown occurs for a range of intermediate values of the rate

https://doi.org/10.1017/S0956792515000364 Published online by Cambridge University Press

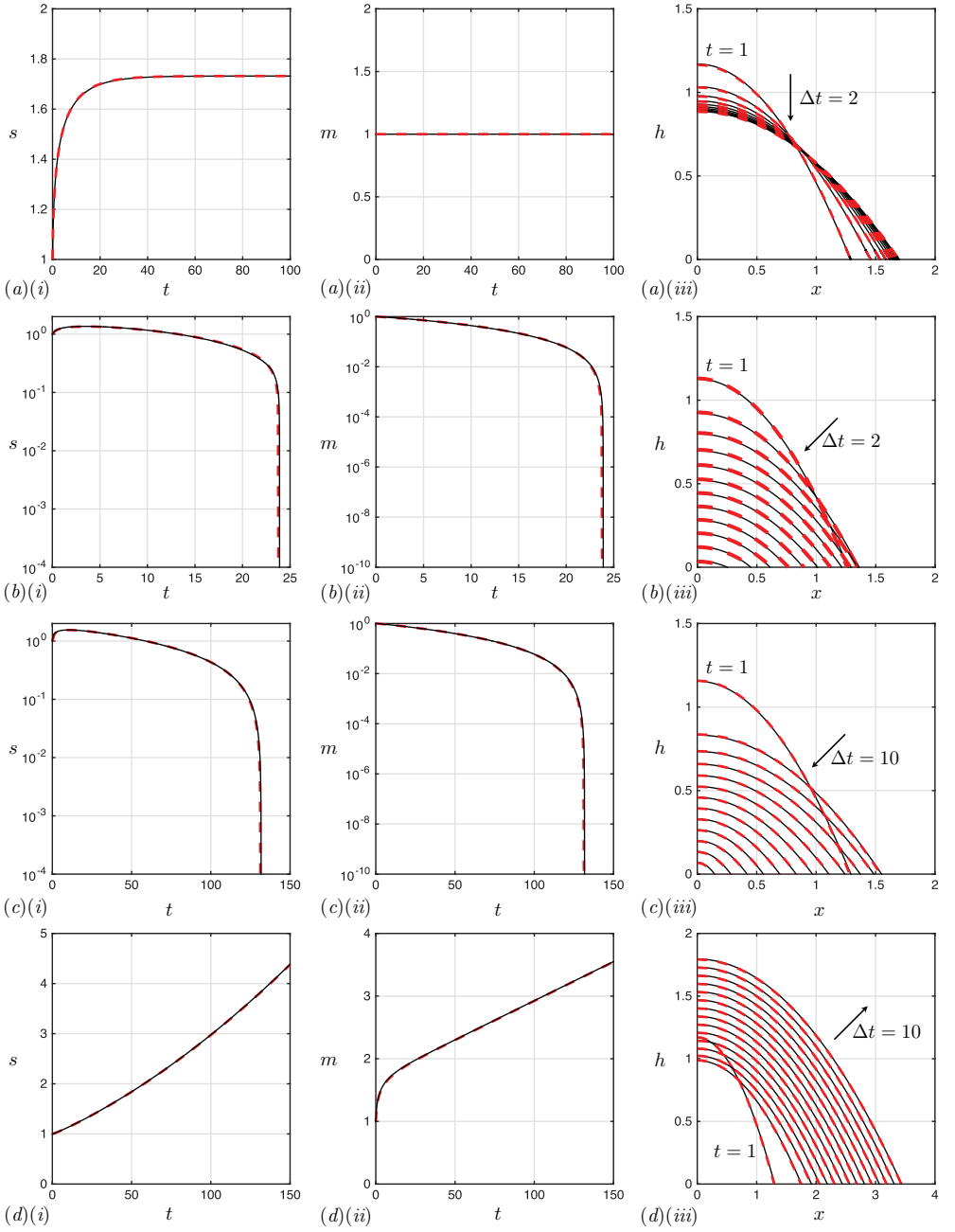

FIGURE 7. Plots for (a) $\mathcal{J} = 0$, (b) $\mathcal{J} = 0.5$, (c) $\mathcal{J} = 0.1$ and (d) $\mathcal{J} = -0.1$. The first, second and third columns contain plots of $s(t)$, $m(t)$ and $h(x, t)$, respectively. In the third column Δt indicates the time between the profiles (we note that Δt is not the time step in our numerical simulations, which is much smaller). The solid lines are extracted from our numerical simulations of equations (5.6)–(5.8) with $n = 1$ and $\lambda = 10^{-5}$ subject to the initial conditions (5.9)–(5.10) with $M = 1$; $m(t)$ is calculated using the trapezium rule. The red-dashed lines are the leading-order asymptotic predictions $s \sim S_0$, $m \sim \Theta_0 S_0^2/3$, $h \sim \Theta_0(S_0^2 - x^2)/(2S_0)$ with $t = T/\epsilon$.

https://doi.org/10.1017/S0956792515000364 Published online by Cambridge University Press

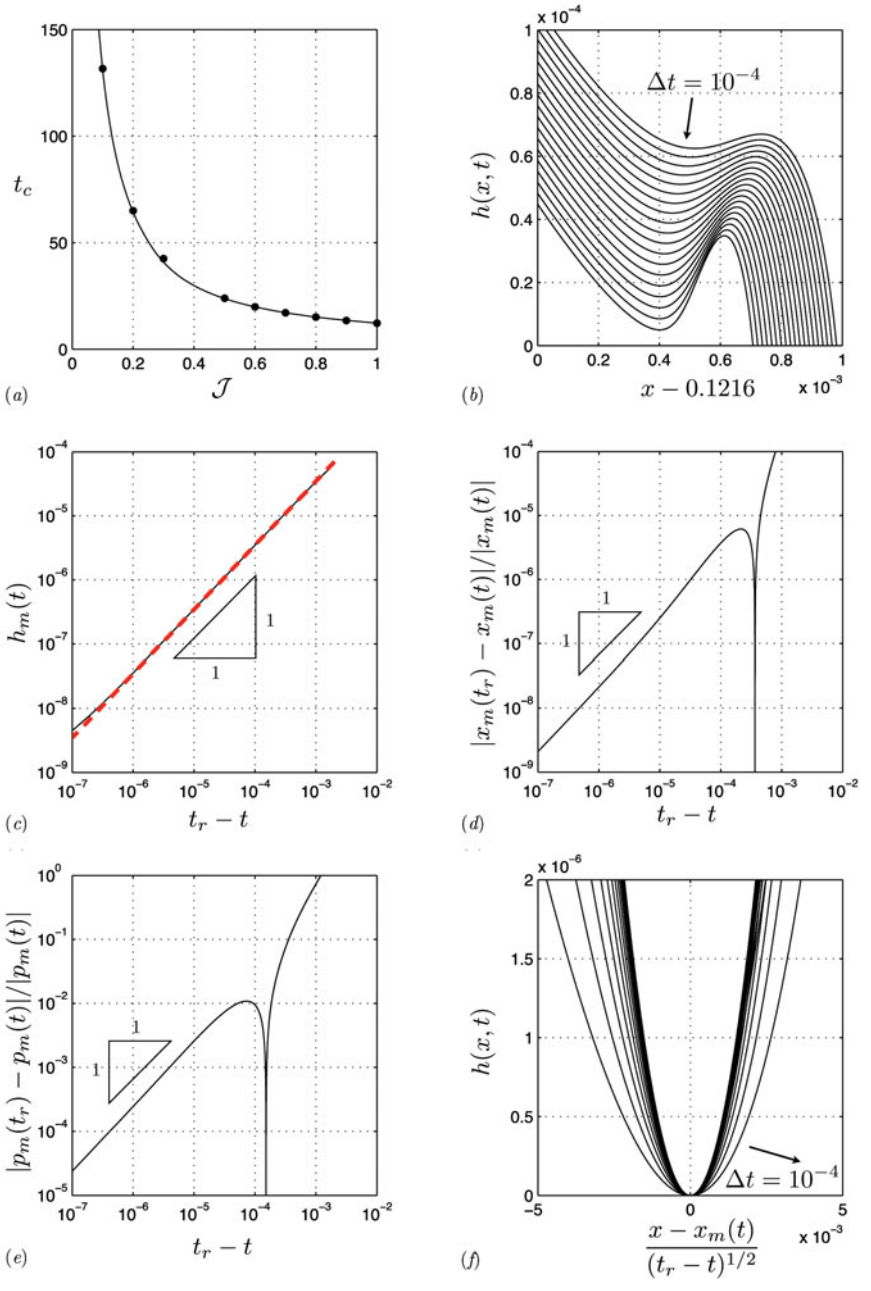

FIGURE 8. (a) Extinction time $t_c \sim T_c \ln(1/\lambda)$ obtained using the leading-order model in Section 3 (solid line) and the numerical simulations of the thin-film problem (5.6)–(5.8) with $n = 1$ and $\lambda = 10^{-5}$ subject to the initial conditions (5.9)–(5.10) with $M = 1$ (solids circles). The other plots are for $\mathcal{J} = 0.4$ showing that the free surface touches down at time $t = t_r \approx 29.906066$ at $x = x_m(t_r) \approx 0.122002 < s(t_r) \approx 0.122285$: (b) film profiles $h(x,t)$ at time intervals of $\Delta t = 10^{-4}$ beginning at $t = 29.904123$; (c) the film thickness $h_m(t) = h(x_m(t),t)$ at the interior minimum at $x = x_m(t)$; (d) $|x_m(t_r) - x_m(t)|/|x_m(t)|$; (e) $|p_m(t_r) - p_m(t)|/|p_m(t)|$, where $p_m(t) = -\partial^2 h/\partial x^2(x_m(t),t)$ is the pressure at the interior minimum; (f) film profiles $h(x,t)$ at time intervals of $\Delta t = 10^{-4}$ beginning at $t = 29.904123$.

https://doi.org/10.1017/S0956792515000364 Published online by Cambridge University Press

of mass transfer $\mathcal{J}$ strictly between 0.3 and 0.5, and that the range of intermediate values of $\mathcal{J}$ for which touchdown occurs appears to decrease with λ. It may be interesting to establish whether or not touchdown is eradicated for sufficiently small values of λ, for other choices of the slip exponent than $n = 1$ and for other initial conditions than equations (5.9)–(5.10). We note that the formation of a rim is reported by [12] in a much more sophisticated axisymmetric model for the evaporation of a liquid drop.

6 Evolution with order-unity mass transfer

We now consider the leading-order evolution of the drop in the distinguished limit considered in Section 4. For $J > 0$, the leading-order outer problem for $h_0(x,t)$ and $s_0(t)$ is given by equations (4.11)–(4.12) subject to the contact-line law (4.5) and the initial condition (4.16), while for $J < 0$ we must impose the additional constraint (4.9), so that the contact-line law becomes equation (4.10). Since the evolution for both $J > 0$ and $J < 0$ is governed by equation (4.11), *i.e.* the thin-film equation *sans* slip, in general it is necessary to solve numerically the leading-order outer problems. This task is severely hampered by the singularities in the drop profile at the contact line, which are quantified by the local expansion (4.14) for $J > 0$ and the local expansion (4.15) for $J < 0$. In particular, the leading-order outer problems are more difficult to solve numerically than the full thin-film problem (2.1)–(2.2) with $n = 1$ and $\lambda \ll 1$. It is for this reason that we do not pursue here the numerical solution of the leading-order outer problems, though this may be a worthwhile task for future research. We shall consider instead the singular parameter limits $J \to 0^{\pm}$ and $J \to \pm\infty$ of both the leading-order outer and inner problems, reconciling thereby the analyses in Sections 3 and 4, as well as self-similar or intermediate asymptotic self-similar solutions of the leading-order outer problems for $J = \mathrm{O}(1)$. We shall compare thereby our asymptotic predictions with numerical simulations of the full problem with $n = 1$ and $\lambda \ll 1$.

6.1 Analysis of the leading-order problems with mass loss

6.1.1 *Small mass loss* $J \to 0^+$

On the slow timescale of contact-line motion and mass loss, namely $\bar{t} = Jt = \mathrm{O}(1)$ as $J \to 0^+$, we expand $h_0 \sim h_{00}$, $\theta_0 \sim \theta_{00}$ and $s_0 \sim s_{00}$ as $J \to 0^+$ to find that the leading-order balance in the outer problem is quasi-steady, with equations (4.11)–(4.12) subject to equation (4.5), as well as equation (4.17), giving

$$h_{00} = \frac{\theta_{00}}{2s_{00}}\left(s_{00}^2 - x^2\right), \quad \frac{\mathrm{d}s_{00}}{\mathrm{d}\bar{t}} = -\frac{1}{\theta_{00}}, \quad \frac{\mathrm{d}}{\mathrm{d}\bar{t}}\left(\frac{\theta_{00}s_{00}^2}{3}\right) = -s_{00}. \qquad (6.1a-c)$$

In the inner region governed by equations (4.1)–(4.2), we find $H_0 \sim -X$ as $J \to 0^+$ except in an exponentially large region in the far field in which the appropriate scalings are given by $X = -\exp(\bar{\xi}/J)$, $H_0 \sim (-X)K_{00}(\bar{\xi},\bar{t})$ as $J \to 0^+$ for $\bar{\xi} > 0$, whereby we recover the boundary-value problem (3.25) with $\bar{t}$ and θ_{00} replacing T and Θ_0, respectively.

The initial conditions for the differential equations (6.1*b*,*c*) are obtained by matching with the solution on the fast timescale in which $t = \mathrm{O}(1)$ as $J \to 0^+$ using a

https://doi.org/10.1017/S0956792515000364 Published online by Cambridge University Press

matched-asymptotic analysis similar to that in Section 3.4: the contact line is pinned and mass transfer absent at leading order as $J \to 0^+$, surface tension driving the drop toward a state of constant mean curvature, giving $\theta_{00}(0) = 3M$ and $s_{00}(0) = 1$, so that

$$\theta_{00} = \left(6M(\bar{t}_c - \bar{t}\,)\right)^{1/2}, \; s_{00} = \left(\frac{2}{3M}(\bar{t}_c - \bar{t}\,)\right)^{1/2}, \; \bar{t}_c = \frac{3M}{2}. \tag{6.2}$$

Thus, the local attractor of the leading-order solution as $J \to 0^+$ takes the form of a self-similar solution in which distances scale with the square-root of the time until extinction on the timescale of mass loss.

The small-J expressions (6.1) and (6.2) are in agreement with the corresponding large-$\mathcal{J}$ expressions (3.3), (3.24) and (5.4) upon identifying $\bar{t}/J$ with T/ϵ. The matched-asymptotic analysis above pertains so long as the sub-inner region is much smaller than the outer region, *i.e.* provided $\epsilon \ll J \ll 1$. As J decreases to $\mathrm{O}(\epsilon)$, the sub-inner region grows in size until it merges into the intermediate region in Section 3.2 when $J = \mathrm{O}(\epsilon)$.

6.1.2 *Large mass loss $J \to +\infty$*

The contact-line motion and mass loss occur on the fast timescale in which $\bar{t} = Jt = \mathrm{O}(1)$ as $J \to +\infty$. Expanding $h_0 \sim h_{00}$ and $s_0 \sim s_{00}$ as $J \to +\infty$, the leading-order balance in the thin-film equation (4.11) becomes

$$\frac{\partial h_{00}}{\partial \bar{t}} = -1 \text{ for } 0 < x < s_{00},$$

so that an application of the initial condition (4.16) gives the solution

$$h_{00}(x, \bar{t}\,) = \mathcal{H}(x) - \bar{t} \text{ for } 0 < x < s_{00}(\bar{t}\,). \tag{6.3}$$

By the boundary condition (4.12*b*), $s_{00}(\bar{t}\,)$ is uniquely determined by the constraint that

$$\mathcal{H}\big(s_{00}(\bar{t}\,)\big) = \bar{t}, \tag{6.4}$$

provided the smooth initial profile $\mathcal{H}(x)$ is strictly decreasing with x. Since the leading-order solution (6.3) corresponds to a rigid-body motion of the free surface with speed J normal to, and toward, the substrate, it satisfies automatically the leading-order versions of the boundary conditions (4.12) provided the initial profile $\mathcal{H}(x)$ satisfies them. The macroscopic contact angle satisfies $\theta_0 \sim \theta_{00}$ as $J \to +\infty$, where $\theta_{00} = -\mathcal{H}'(s_{00}(\bar{t}\,))$ by equation (6.3). It follows from differentiation of equation (6.4) that

$$\frac{\mathrm{d}s_{00}}{\mathrm{d}\bar{t}} = \frac{1}{\mathcal{H}'(s_{00})} = -\frac{1}{\theta_{00}}, \tag{6.5}$$

so that the leading-order version of the contact-line law (4.5) is also satisfied automatically. The solution (6.3)–(6.4) serves thereby as a concrete illustration of the physical significance of the contact-line law (4.5), as discussed in Section 4.

As $J \to +\infty$ in the inner region governed by equations (4.1)–(4.2), $H_0 \sim \theta_{00}(-X)$ except in an algebraically small sub-inner region at the contact line in which the appropriate

https://doi.org/10.1017/S0956792515000364 Published online by Cambridge University Press

scalings are given by $X = J^{-1/(3-n)}\overline{X}$, $H_0 \sim J^{-1/(3-n)}H_{00}$, whereby

$$H_{00}^n \frac{\partial^3 H_{00}}{\partial \overline{X}^3} = -\frac{H_{00}}{\theta_{00}} - \overline{X} \text{ for } \overline{X} < 0, \tag{6.6}$$

with

$$H_{00} = 0,\ -\frac{\partial H_{00}}{\partial \overline{X}} = 1 \text{ on } \overline{X} = 0^-; \quad H_{00} \sim \theta_{00}\left(-\overline{X}\right) \text{ as } \overline{X} \to -\infty. \tag{6.7}$$

A degree-of-freedom count reveals that the sub-inner problem (6.6)–(6.7) is correctly specified, there being two oscillatory exponentially decaying contributions in the far field.

For future reference, we note that, if $\mathcal{H}(x) \sim \bar{t}_c - \left(x/\alpha\right)^m$ as $x \to 0$, where $\bar{t}_c$, α and m are prescribed positive constants, with $m = 2$ or $m > 3$ being required for there to be no flux through the line of symmetry, then $s_{00} \sim \alpha(\bar{t}_c - \bar{t})^{1/m}$ as $\bar{t} \to \bar{t}_c^-$ and the extinction time $t_c \sim \bar{t}_c/J$ as $J \to +\infty$. It follows that, since the case $m = 2$ is for the usual reasons the generic one, in general the local attractor of the leading-order solution as $J \to +\infty$ takes the form of a self-similar solution in which distances scale with the square-root of the time until extinction on the timescale of mass loss.

6.1.3 *Non-existence of self-similar solutions for $J = O(1)$*

Motivated by the existence of self-similar scaling behaviour near extinction for both small and large J, we now seek a self-similar solution of equations (4.11)–(4.12) subject to equations (4.5) for $J > 0$ with $J = \mathrm{O}(1)$. We find, however, that the only candidate takes form

$$h_0 = \tau J f(\eta),\ s_0 = \eta_0 \tau,\ \eta = \frac{x}{\eta_0 \tau},\ \tau = t_c - t, \tag{6.8}$$

where η_0 is a positive constant that we define below and t_c is the extinction time. We obtain thereby the nonlinear fourth-order ordinary differential equation

$$-f + \eta f' + \frac{1}{\alpha}\left(f^3 f'''\right)' = -1 \text{ for } 0 < \eta < 1, \tag{6.9}$$

with

$$f'(0) = 0,\ f'''(0) = 0,\ f(1) = 0,\ f'(1) = -1, \tag{6.10}$$

where $\alpha > 0$ is to be determined as part of the solution to equations (6.9)–(6.10), the constants η_0 and θ_0 then being determined in terms of J and α by the expressions $\eta_0 = \left(\alpha J^3\right)^{1/4}$ and $\theta_0 = \left(J/\alpha\right)^{1/4}$. We note that it would follow from equations (6.9)–(6.10) that

$$\int_0^1 f(\eta) = \frac{1}{2}, \tag{6.11}$$

an expression representing global conservation of mass. The local expansions of $f(\eta)$ near the line of symmetry and contact line may be extracted from equations (4.13) and (4.14). They contain three degrees of freedom in addition to α, giving a total of four degrees of freedom, so that the problem (6.9)–(6.10) for $f(\eta)$ and α appears to be correctly specified. However, we have been unable to find a solution numerically. That equations (6.9)–(6.10) do not appear to have a solution is consistent with the small- and large-J analyses in

https://doi.org/10.1017/S0956792515000364 Published online by Cambridge University Press

Sections 6.1.1–6.1.2 and with our numerical simulations of the full thin-film problem with $n = 1$ and $\lambda \ll 1$ in Section 6.1.5.

6.1.4 *Asymptotically self-similar behaviour for $J = O(1)$*

Motivated by the apparent non-existence of a self-similar solution in Section 6.1.3 and the large-J analysis in Section 6.1.2 in which the balance $\partial h_0/\partial t \sim -J$ pertains in the outer region, we now seek for $J > 0$ an intermediate-asymptotic solution of the leading-order outer problem of the form

$$h_0 \sim \tau F(\eta),\ s_0 \sim \eta_0 \tau^{1/m},\ \eta = \frac{x}{\tau^{1/m}},$$

as $\tau = t_c - t \to 0^+$, where, on physical grounds, η_0 and m are expected to be positive constants. Since

$$\frac{\partial h_0}{\partial t} \sim -F + \frac{\eta}{m}F',\ \frac{\partial}{\partial x}\left(h_0^3 \frac{\partial^3 h_0}{\partial x^3}\right) \sim \tau^{4(m-1)/m}(F^3F''')' \text{ as } \tau \to 0^+,$$

we deduce that, provided $m > 1$,

$$-F + \frac{\eta}{m}F' = -J \text{ for } 0 < \eta < \eta_0, \tag{6.12}$$

at leading order as $\tau \to 0^+$. It is readily shown that the solution of equation (6.12) subject to the leading-order version of the boundary condition (4.12*c*), namely $F(\eta_0) = 0$, is given by

$$F(\eta) = J\left(1 - \frac{\eta^m}{\eta_0^m}\right). \tag{6.13}$$

This solutions satisfies the leading-order versions of the boundary conditions (4.12*a*,*d*) and the contact-line law (4.5), but the flux condition (4.12*b*) only if $m = 2$ or $m > 3$. Since m is thus far indeterminate in this sense, it is essential to analyse the boundary layer near $x = 0$ in which the scalings $h_0 \sim J\tau + \tau^m G(\xi)$, $\xi = x/\tau$ pertain as $\tau \to 0^+$, whereby

$$J^3 G'''' + \xi G' - mG = 0 \text{ for } \xi > 0, \tag{6.14}$$

with

$$G'(0) = G'''(0) = 0,\ G(\xi) \sim -\frac{J\xi^m}{\eta_0^m} \text{ as } \xi \to \infty. \tag{6.15}$$

An application of the Liouville–Green (JWKB) method as $\xi \to \infty$ identifies the only acceptable exponentially decaying contribution to G to have $\ln G \sim -3\xi^{4/3}/4J$ as $\xi \to \infty$ (this relates to the variable τ being of backward time, in contrast to the forward similarity solution addressed Section 6.2.3 in which two oscillatory exponentially decaying contributions are admissible); a boundary-condition count then implies that m should be viewed as an eigenvalue (with η_0 an arbitrary constant corresponding to the eigenfunction being of arbitrary amplitude), whose values can readily seen to be given by the positive

https://doi.org/10.1017/S0956792515000364 Published online by Cambridge University Press

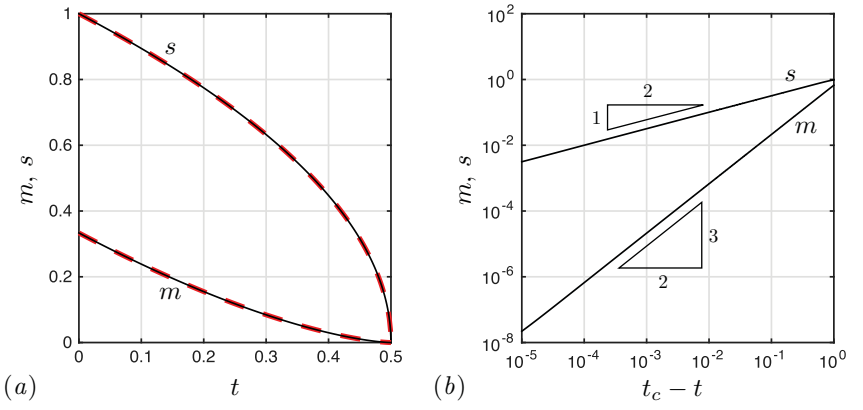

FIGURE 9. Plots of $s(t)$ and $m(t)$ for (a) $M = 1/3$ and (b) $M = 1$. The solid lines are extracted from the numerical solution of equations (5.6)–(5.8) with $n = 1$ and $\lambda = 10^{-5}$ subject to the initial conditions (5.9)–(5.10). The red-dashed lines in (a) are extracted from the exact solution (6.16).

even integers, with

$$m = 2 \qquad G(\xi) = -J\xi^2/\eta_0^2,$$
$$m = 4 \qquad G(\xi) = -J\xi^4/\eta_0^4 - 6J^4/\eta_0^4,$$
$$\text{etc.}$$

The case $m = 2$ is the generic one and corresponds to the exact solution

$$h_0(x,t) = J\left(t_c - t - \frac{x^2}{\alpha^2}\right), \quad s_0(t) = \alpha(t_c - t)^{1/2}, \tag{6.16}$$

of the leading-order outer problem (4.11)–(4.12) subject to the constraint (4.5), which is valid for all $t_c > 0$ and $\alpha > 0$. In the exact solution (6.16) the film profile is a parabola moving with speed J normal to, and toward, the substrate, corresponding in the thin-film limit to the mean curvature, and hence the pressure, being constant.

6.1.5 *Comparison of asymptotic and numerical predictions*

The plots of $s(t)$ and $m(t)$ in Figure 9(a) show excellent visual agreement between the exact solution (6.16) and the numerical solution of equations (5.6)–(5.8) with $J = 1$, $\lambda = 10^{-5}$ and the initial condition given by equations (5.9)–(5.10) with $M = 1/3$ (corresponding to $A = 1/2$, $B = 0$). This agreement provides further quality control for the validity of the small-slip asymptotics in Section 4. For other initial conditions of the form (5.9)–(5.10) with $B \neq 0$, in which the initial profile is not a parabola, we find that our numerical predictions for the scaling behaviour near extinction of both $s(t)$ and $m(t)$ are consistent with those corresponding to the exact solution (6.16). For example, we plot the numerical predictions for $M = 1$ (corresponding to $A = -3/14$, $B = 10/7$) in Figure 9(b), showing agreement over at least four decades near to the extinction time, t_c.

https://doi.org/10.1017/S0956792515000364 Published online by Cambridge University Press

6.2 Analysis of the leading-order problems with mass gain

6.2.1 *Small mass gain $J \to 0^-$*

On the slow timescale of contact-line motion and mass gain in which $\bar{t} = |J|t = \mathrm{O}(1)$ as $J \to 0^-$, we expand $h_0 \sim h_{00}$ and $\theta_0 \sim \theta_{00}$ as $J \to 0^-$ to find that the leading-order outer balance is again quasi-steady, with the governing equations (4.11)–(4.12) subject to the constraint (4.5) giving equation (6.1*a*) with $s_{00} = 1 + \bar{t}$. The leading-order macroscopic contact angle θ_{00} is then determined by the leading-order version of the expression (4.17) representing global conservation of mass, namely

$$\frac{\mathrm{d}}{\mathrm{d}\bar{t}}\left(\frac{\theta_{00}s_{00}^2}{3}\right) = s_{00}. \tag{6.17}$$

In order to satisfy the leading-order version of the boundary condition (4.12*c*) subject to the constraint (4.9) that $\theta_0 = 1$, it is necessary to introduce an exponentially narrow region near to the contact line in which the appropriate scalings are given by $s_0 - x = \exp(\xi/J)$, $h_0 \sim (s_0 - x)K_{00}(\xi, t)$ as $J \to 0^-$ for $\xi > 0$, whereby we recover the boundary-value problem (3.23) with $\bar{t}$ and θ_{00} replacing T and Θ_0, respectively.

The initial condition for the differential equation (6.17) with $s_{00} = 1 + \bar{t}$ is obtained by matching with the solution on the fast timescale in which $t = \mathrm{O}(1)$ as $J \to 0^-$ using a matched-asymptotic analysis similar to that in Sections 3.4 and 6.1.1, revealing that $\theta_{00}(0) = 3M$, and hence that θ_{00} is given by equation (5.5) upon replacing Θ_0 and $\overline{T}$ with θ_0 and $\bar{t}$, respectively. Thus, the small $J < 0$ and large $\mathcal{J} < 0$ predictions for the drop profile, the macroscopic contact angle and the contact-line velocity are in agreement, and the long-time attractor of the leading-order solution as $J \to 0^-$ takes the form of a self-similar solution in which distances scale linearly with time.

The matched-asymptotic analysis above pertains so long as $\epsilon \ll |J| \ll 1$, the sub-outer region then being much larger than the inner region in Section 4.1. As $-J$ decreases to $\mathrm{O}(\epsilon)$, the sub-outer region shrinks in size until it merges into the intermediate region in Section 3.2 when $-J = \mathrm{O}(\epsilon)$.

6.2.2 *Large mass gain $J \to -\infty$*

On the fast timescale in which $\bar{t} = |J|t = \mathrm{O}(1)$ as $J \to -\infty$, we expand $h_0 \sim h_{00}$ and $\theta_0 \sim \theta_{00}$ as $J \to -\infty$ to find that the thin-film equation (4.11) becomes

$$\frac{\partial h_{00}}{\partial \bar{t}} = 1 \text{ for } 0 < x < 1 + \bar{t}.$$

The boundary condition (4.12*c*) and the initial condition (4.16) imply that the pertinent boundary data are given by $h_{00}(x, 0) = \mathcal{H}(x)$ for $0 < x < 1$ and $h_{00}(1 + \bar{t}, \bar{t}) = 0$ for $\bar{t} > 0$, so that the leading-order solution is given by

$$h_{00}(x, \bar{t}) = \begin{cases} \mathcal{H}(x) + \bar{t} & \text{for } 0 < x < 1, \\ 1 + \bar{t} - x & \text{for } 1 < x < 1 + \bar{t}. \end{cases} \tag{6.18}$$

https://doi.org/10.1017/S0956792515000364 Published online by Cambridge University Press

Since this solution corresponds to a rigid-body motion of the free surface, it satisfies automatically the leading-order versions of the boundary conditions (4.12) subject to the constraint (4.9) that $\theta_0 = 1$ (again assuming the initial profile $\mathcal{H}(x)$ to satisfy (4.12) with $\theta_0(0) = 1$). If $\mathcal{H}(x) \sim (1-x) + \alpha(1-x)^m$ as $x \to 1^-$, where α and m are prescribed real constants with $m > 1$, then there is a boundary layer at $x = 1$ in which the scalings $x = 1 + |J|^{-1/4}X$, $h_0 \sim \bar{t} - |J|^{-1/4}X + |J|^{-m/4}\bar{t}^m F(\eta)$, $\eta = X/t$ pertain as $J \to -\infty$, whereby

$$mF - \eta F' + F'''' = 0 \text{ for } -\infty < \eta < \infty,$$

with

$$F(\eta) \sim \alpha(-\eta)^m \text{ as } \eta \to -\infty, \quad F(\eta) \to 0 \text{ as } \eta \to +\infty,$$

a boundary-value problem that may be readily solved using a Fourier transform. The boundary layer grows in size until its length is of order unity, and hence this asymptotic structure breaks down when $\bar{t} = \mathrm{O}(|J|^{1/4})$.

On the timescale in which $T = |J|^{-1/4}\bar{t} = \mathrm{O}(1)$ (corresponding to t being of $\mathrm{O}(|J|^{-3/4})$), we scale $x = |J|^{1/4}X$ and $h_0 = |J|^{1/4}H_0$ to deduce that

$$H_0 \sim T - X \text{ for } 0 < X < T \text{ as } J \to -\infty, \tag{6.19}$$

except in a boundary layer near the origin in which $h_0 \sim |J|^{1/4}T + H_{00}(x, T)$, whereby

$$\frac{\partial H_{00}}{\partial T} + T^3 \frac{\partial^4 H_{00}}{\partial x^4} = 0 \text{ for } 0 < x < \infty,$$

with

$$\frac{\partial H_{00}}{\partial x} = 0, \ \frac{\partial^3 H_{00}}{\partial x^3} = 0 \text{ at } x = 0; \quad H_{00} \sim -x \text{ as } x \to \infty.$$

Matching with the fast timescale above implies that the initial condition is given by

$$H_0(x, 0) = \begin{cases} \mathcal{H}(x) & \text{for } 0 < x < 1, \\ 1 - x & \text{for } x > 1. \end{cases}$$

A standard application of Fourier-transform techniques to the even extension of H_{00} into $x < 0$ reveals that the solution may be written in the form

$$H_{00}(x, T) = T\mathcal{F}\left(\frac{x}{T}\right) + 1 + \frac{1}{\pi}\int_0^\infty \int_0^1 \big(\mathcal{H}(u) - (1-u)\big)\cos(uv)\cos(vx)\mathrm{e}^{-v^4T^4/4}\,\mathrm{d}u\mathrm{d}v,$$

where

$$\mathcal{F}(\zeta) = -\frac{2}{\Gamma(1/4)} - \frac{2}{\pi}\int_0^\infty \left(\frac{1-\cos(u\zeta)}{u^2}\right)\mathrm{e}^{-u^4/4}\,\mathrm{d}u. \tag{6.20}$$

An application of Laplace's method then gives

$$H_{00}(X, T) \sim T\mathcal{F}\left(\frac{x}{T}\right) + 1 + \frac{(2M-1)}{4T}\mathcal{P}\left(\frac{x}{T}\right) \text{ as } T \to \infty \text{ with } \frac{x}{T} = \mathrm{O}(1), \tag{6.21}$$

where

$$\mathcal{P}(\zeta) = -\mathcal{F}'(\zeta) = \frac{2}{\pi}\int_0^\infty \cos(u\zeta)\mathrm{e}^{-u^4/4}\,\mathrm{d}u; \tag{6.22}$$

https://doi.org/10.1017/S0956792515000364 Published online by Cambridge University Press

for future reference we note that $\mathcal{P}(\zeta)$ is a solution of the third-order Airy-type equation $\mathcal{P}''' = \zeta\mathcal{P}$ that decays exponentially in the far-field, the method of steepest descents giving

$$\mathcal{P}(\zeta) \sim \sqrt{\frac{2}{3\pi}}|\zeta|^{-1/3}\exp\left(-\frac{3}{8}|\zeta|^{4/3}\right)\cos\left(\frac{\sqrt{27}}{8}|\zeta|^{4/3}-\frac{\pi}{6}\right) \text{ as } |\zeta|\to\infty. \tag{6.23}$$

It follows from equations (6.19) and (6.21) that, as for small mass loss in Section 6.2.1, the long-time attractor of the leading-order solution as $J \to -\infty$ takes the form of a self-similar solution in which distances scale linearly with time.

6.2.3 *Self-similar solution for $J = O(1)$*

Motivated by the large-time linear scaling behaviour for both small and large J in Sections 6.2.1–6.2.2, we now seek a self-similar solution of the first kind of the moving-boundary problem (4.11)–(4.12) subject to the constraints (4.9) and (4.10), which is readily shown to take the form

$$h_0 = \tau|J|f(\eta),\ s_0 = |J|\tau,\ \eta = \frac{x}{|J|\tau},\ \tau = t + t_0,$$

where t_0 is an arbitrary constant. We obtain thereby the nonlinear fourth-order ordinary differential equation

$$f - \eta f' + \frac{1}{|J|}\left(f^3 f'''\right)' = 1 \text{ for } 0 < \eta < 1, \tag{6.24}$$

with

$$f'(0) = 0,\ f'''(0) = 0,\ f(1) = 0,\ f'(1) = -1. \tag{6.25}$$

We note that the expression representing global conservation of mass is again given by equation (6.11). The local expansions of $f(\eta)$ near the line of symmetry and contact line may be extracted from equations (4.13) and (4.15). They contain a total of four degrees of freedom, so that the problem (6.24)–(6.25) for $f(\eta)$ is correctly specified. The numerical solution of equations (6.24)–(6.25) is hindered by the singularities at the contact line implicit in equation (4.15). One method to deal with these singularities involves truncating the domain to $\eta \in [0, 1-\varepsilon]$ and using the local expansion (4.15) to impose appropriate boundary conditions at $\eta = 1-\varepsilon$, where $0 < \varepsilon \ll 1$. We found it easier to solve numerically the regularised problem

$$2g_\varepsilon - \eta g_\varepsilon' + \frac{1}{|J|}\left((g_\varepsilon')^3 + \varepsilon^3\right) g_\varepsilon'''' = \eta \text{ for } 0 < \eta < 1, \tag{6.26}$$

with

$$g_\varepsilon(0) = 0,\ g_\varepsilon''(0) = 0,\ g_\varepsilon'(1) = 0,\ g_\varepsilon''(1) = -1. \tag{6.27}$$

A formal asymptotic analysis implies that $g_\varepsilon' \sim f$ as $\varepsilon \to 0$ except in a boundary layer at $\eta = 1$ in which $g_\varepsilon'(\eta) \sim 1 - \eta$ as $\varepsilon \to 0$ with $1 - \eta = \mathrm{O}(\varepsilon)$. We note that it is advantageous to work with g_ε because it has a weaker singularity than g_ε' at $\eta = 1$.

We use *bvp5c* in MATLAB to solve equations (6.26)–(6.27) using continuation in the parameter ε, with absolute and relative error tolerances of 10^{-12}. Figure 10(a) illustrates

https://doi.org/10.1017/S0956792515000364 Published online by Cambridge University Press

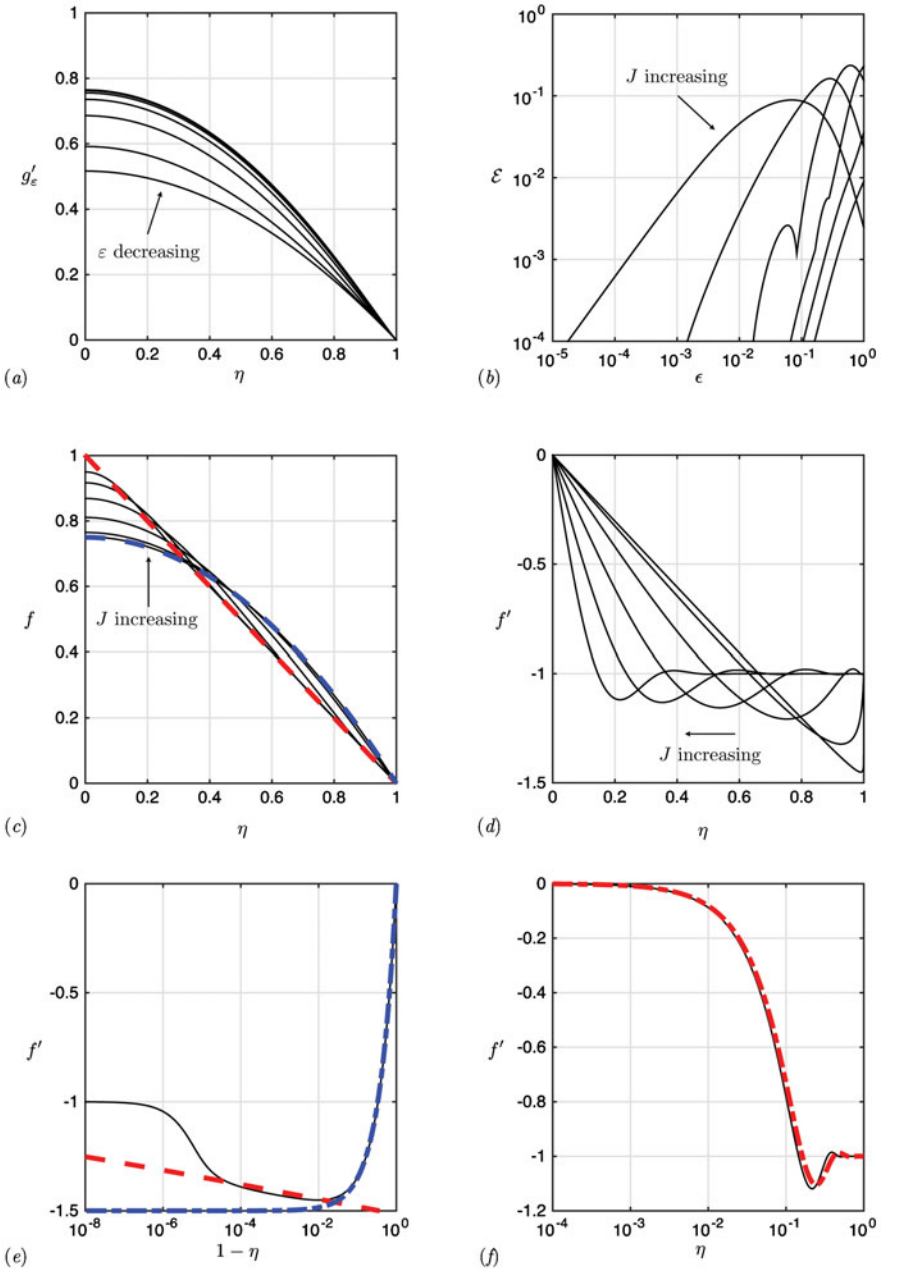

FIGURE 10. (*a*) Plot of $g'_\varepsilon(\eta)$ for $J=-1$ and $\varepsilon = 10^{-m/3}$, $m = 0, 1, \ldots, 9$ (the lines are indistinguishable for $m \geqslant 6$). Plot of (*b*) $\mathcal{E}(\varepsilon)$ for $J=-10^n$, $n=-1, 0, 1, 2, 3, 4$ (calculated from the discrete version of (6.28) using 1000 uniformly spaced grid points). Plot of (*c*) $f(\eta) \approx g'_\varepsilon(\eta)$ and (*d*) $f'(\eta) \approx g''_\varepsilon(\eta)$ for $J=-10^n$, $n=-1, 0, 1, 2, 3, 4$, with $\mathcal{E}(\varepsilon) < 10^{-4}$ for each J; (*c*) also contains plots of $1-\eta$ (red-dashed line) and $3(1-\eta^2)/4$ (blue-dashed line). (*e*) Plot of $f'(\eta) \approx g''_\varepsilon(\eta)$ for $\varepsilon = 10^{-5}$ (solid line), of $-3\eta/2$ (blue-dashed line) and of $-G(\xi) - JG'(\xi)$, $\eta = 1-\exp(\xi/J)$ obtained from the solution of (6.29) (red-dashed line) for $J=-0.1$. (*f*) Plot of $f'(\eta) \approx g''_\varepsilon(\eta)$ for $\varepsilon^3 = 10^{-5}$ (solid line) and of $\mathcal{F}'(\zeta)$, $\eta = \zeta/|J|^{1/4}$ obtained from (6.20) (red-dashed line) for $J=-10^4$.

https://doi.org/10.1017/S0956792515000364 Published online by Cambridge University Press

the convergence of g_ε' as $\varepsilon \to 0$ for $J = -1$, while Figure 10(b) shows that the relative error,

$$\mathcal{E}(\varepsilon) := \frac{\max_{\eta\in[0,1]} |g_{10\varepsilon}(\eta) - g_\varepsilon(\eta)|}{\max_{\eta\in[0,1]} |g_\varepsilon(\eta)|}, \tag{6.28}$$

decreases with ε at a rate that increases with $-J$. For each J we decrease ε until the relative error is no larger than 10^{-4} and plot the resulting predictions for $f \approx g_\varepsilon'$ and $f' \approx g_\varepsilon''$ in Figures 10(c) and (d), which illustrates that as $-J$ increases the drop profile undergoes a transition from having constant non-zero curvature as $J \to 0^-$ to being almost linear as $J \to -\infty$. This behaviour is consistent with the leading-order outer behaviour on the timescale of mass loss in Section 6.2.1 (as $J \to 0^-$) and Section 6.2.2 (as $J \to -\infty$), and can be confirmed by a similar matched-asymptotic analysis of equations (6.24)–(6.25), as we shall now briefly describe.

As $J \to 0^-$, $f \sim 3(1-\eta^2)/4$ except in an exponentially narrow boundary layer at $\eta = 1$ in which the appropriate scalings are given by $1 - \eta = \exp(\xi/J)$, $f(\eta) \sim (1-\eta)G(\xi)$ for $\xi > 0$, whereby

$$G^3 G' = 1 - G \text{ for } \xi > 0; \quad G(0^+) = \frac{3}{2}, \; G(\infty) = 1. \tag{6.29}$$

The resulting predictions for the profile and slope are in good agreement with our numerical simulations of equations (6.26)–(6.27) even for moderate values of J, as illustrated in Figures 10(c) and (e) for $J = -0.1$. We note that our numerical simulations are consistent with our regularisation, with $f'(\eta) \approx g_\varepsilon''(\eta) \sim -1$ as $\varepsilon \to 0$ with $1 - \eta = \mathrm{O}(\varepsilon)$ in Figure 10(e).

As $J \to -\infty$, $f \sim 1 - \eta$ except in a boundary layer at $\eta = 0$ in which the appropriate scalings are given by $\eta = |J|^{-1/4}\zeta$, $f(\eta) \sim 1 + |J|^{-1/4}\mathcal{F}(\zeta)$, whereby

$$\mathcal{F} - \zeta\mathcal{F}' + \mathcal{F}''' = 0 \text{ for } \zeta > 0; \quad \mathcal{F}'(0) = 0, \; \mathcal{F}''(0) = 0, \; \mathcal{F}(\zeta) \sim -\zeta \text{ as } \zeta \to \infty.$$

A standard application of Fourier-transform techniques to the even extension of $\mathcal{F}$ into $\zeta < 0$ reveals that the solution is given by equation (6.20). Hence, we recover in the limit $J \to -\infty$ exactly the long-time attractor of the leading-order solution as $J \to -\infty$ found in Section 6.2.2. The resulting predictions for the profile and slope are in good agreement with our numerical simulations of equations (6.26)–(6.27) for large values of $-J$, as illustrated in Figures 10(c) and (f) for $J = -10^4$. We note that in the boundary layer the pressure

$$p_0 = -\frac{\partial^2 h_0}{\partial x^2} = -\frac{1}{|J|\tau} f''(\eta) \sim \frac{1}{|J|^{3/4}\tau}\mathcal{P}(\zeta) \text{ as } J \to -\infty,$$

where $\mathcal{P}(\zeta)$ is given by equation (6.22), the far-field behaviour (6.23) being consistent with the presence of weak capillary ripples in Figure 10(f).

That the boundary layer is exponentially narrow and located at the contact line for small $-J$, but only algebraically narrow and located on the line of symmetry for large $-J$, explains why our numerical simulations converge more rapidly for large $-J$ than for small $-J$, as illustrated in Figure 10(b).

https://doi.org/10.1017/S0956792515000364 Published online by Cambridge University Press

6.2.4 *Comparison of asymptotic and numerical predictions*

The plot in Figure 11(a)(*i*) shows that the appropriately scaled drop profiles obtained from the numerical solution of equations (5.6)–(5.8), with $J = -1$, $\lambda = 10^{-5}$ and the initial condition given by equations (5.9)–(5.10) with $M = 1/3$, tend at large times to the film profile predicted by the numerical solution of equations (6.26)–(6.27), with $J = -1$ and ε selected as in Section 6.2.3. The plot in Figure 11(a)(*ii*) of the contact-line velocity predicted by the numerical simulations of the thin-film problem are in excellent agreement with the prediction of the small-slip asymptotics that $\dot{s} = -J + \mathrm{O}(\lambda)$ as $\lambda \to 0$. This agreement provides further quality control for the validity of the small-slip asymptotics in Section 4. We find good agreement for other initial conditions of the form (5.9)–(5.10) with $M \neq 1/3$ provided the initial rate of change of curvature, $\mathcal{H}'''(x) = -45(M - 1/3)x$, is not too large. For $M = 1$, we find that, while the drop profiles tend at large times to those of the similarity solution, as illustrated in Figure 11(b)(*i*), the leading-order prediction for the contact-line velocity is violated between approximately $t = 10^{-2}$ and $t = 1$, and it appears that the rapid surface-tension-driven relaxation of the initial profile causes the velocity to deviate substantially from $-J$ in an oscillatory manner, as illustrated in Figure 11(b)(*ii*). Our numerical simulations suggest that the amplitude and duration of the oscillations both decrease with λ, as illustrated in Figure 11(b)(*iii*), though we do not have a convincing explanation for this deviation and do not pursue it further here.

7 Discussion

In this paper, we have investigated the effects of mass transfer on a moving contact line. The aim was to gain the physical insight afforded by an asymptotic analysis of the effect of the simplest possible mass-transfer mechanism on the simplest possible model of contact-line motion. In Section 2, we formulated the dimensionless thin-film problem (2.1)–(2.2) governing the evolution of a two-dimensional drop of thickness $h(x, t)$ and drop half-width $s(t)$. The model contains only three dimensionless parameters: the slip coefficient, λ; the slip exponent, n, with $n < 3$ being required for contact-line motion; and the rate of mass transfer J, with $J > 0$ corresponding to mass loss and $J < 0$ to mass gain. We emphasise that the modelling assumptions leading to equations (2.1)–(2.2) are gross simplifications of the complex physics governing the evaporation or condensation of a sessile liquid drop. In particular, we have assumed the drop to be partially wetting, the contact-line motion to be regularised by a generalised slip law and the mass transfer to be large, uniform and restricted to the contact set in the cases of both mass loss and mass gain (we note that the model is relevant in other contexts, as described in Section 1). However, consideration of such a simple possible model facilitates an almost complete understanding of the (surprisingly rich) dynamics governing the evolution of the drop on the timescale of mass transfer and, perhaps more importantly, of the asymptotic and numerical methodologies required to understand them. Our hope is that such insight may be helpful in more sophisticated models, as has been the case for thin-film models of drop spreading in the absence of mass transfer. (There the contact-line motion depends at leading order only weakly on the choice of regularisation provided the length scale of the regularisation is much smaller than that of the drop (in the sense that Tanner's law

https://doi.org/10.1017/S0956792515000364 Published online by Cambridge University Press

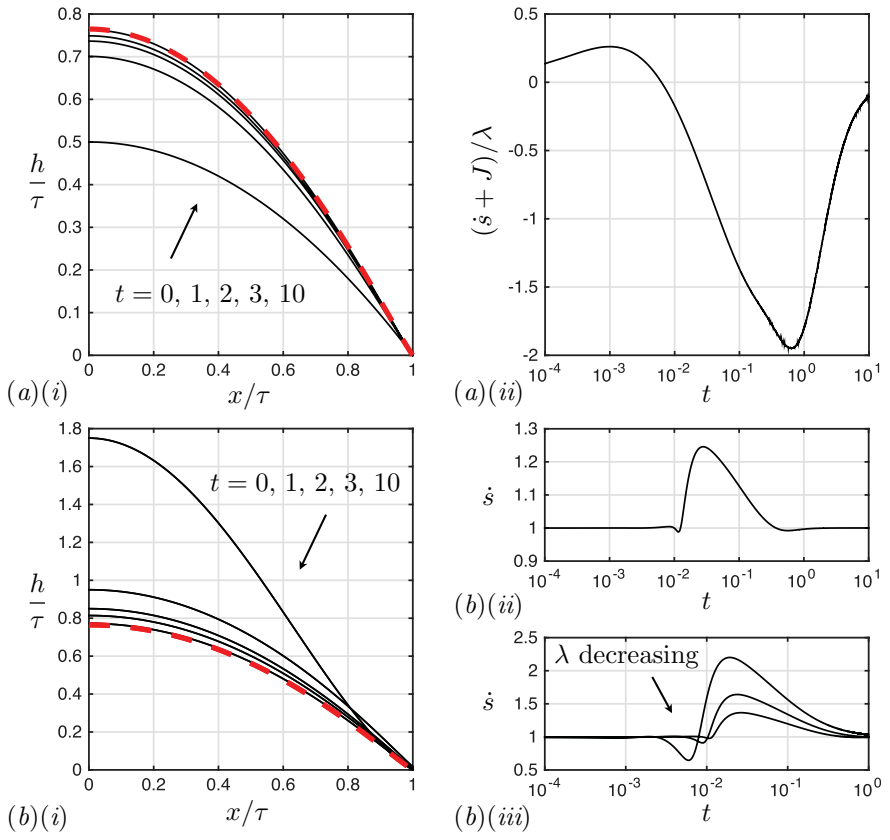

FIGURE 11. Plot showing the scaled drop profile (solid lines) tending at large times to the similarity solution (red-dashed line) for (a)(*i*) $M = 1/3$ and (b)(*i*) $M = 1$, with $\lambda = 10^{-5}$ and $\tau = t + s(10) - 10$; (a)(*ii*) plot showing $\dot{s} = -J + \mathrm{O}(\lambda)$ for $M = 1/3$ with $\lambda = 10^{-5}$; plot of $\dot{s}$ for (b)(*ii*) $\lambda = 10^{-5}$ and (b)(*iii*) $\lambda = 10^{-3}$, 10^{-4} and 10^{-5}. The solid lines are extracted from the numerical solution of equations (5.6)–(5.8) with $n = 1$ and $J = -1$ subject to the initial conditions (5.9)–(5.10). The similarity solution is extracted from the numerical solution of equations (6.26)–(6.27).

depends only logarithmically on the ratio of these length scales); see, for example, [23]). There is a burgeoning field seeking to understand the effects of mass transfer on contact-line motion within the thin-film framework, and, in particular, how the hydrodynamics of contact-line motion (embodied in Tanner's law) is modified by the presence of mass transfer and whether or not there are any universal aspects to the dynamics as in the absence of mass transfer. We used the method of matched asymptotic expansions to analyse systematically the thin-film problem (2.1)–(2.2) in the small-slip limit in which $\lambda \to 0$. Our analysis revealed that the leading-order outer formulation and contact-line law that are selected in the small-slip limit depend delicately on both the size and sign of the rate of mass transfer J, with the kinematics of mass transfer modifying the usual hydrodynamics at sufficiently small values, but dominating it at sufficiently large values.

In Section 3 we showed that, in the distinguished limit in which mass transfer is small in the sense that $\mathcal{J} = J \ln(1/\lambda) = \mathrm{O}(1)$ as $\lambda \to 0$, the spatial asymptotic structure selected

https://doi.org/10.1017/S0956792515000364 Published online by Cambridge University Press

in the small-slip limit is the same in the presence of mass transfer as in its absence, the timescale of contact-line motion being given by $T = t/\ln(1/\lambda) = \mathrm{O}(1)$ as $\lambda \to 0$. We showed that the leading-order outer formulation is quasi-steady and governed by the pair of nonlinear ordinary differential equations (3.4) and (3.16) for the leading-order half-drop width $S_0(T)$ and macroscopic contact angle $\Theta_0(T)$, (3.4) representing global conservation of mass and equation (3.16) being a generalisation of Tanner's law that takes into account mass transfer. In the case of mass gain ($\mathcal{J} < 0$), we showed that the contact-line law (3.16) has qualitatively the same shape as Tanner's law. However, in the case of mass loss ($\mathcal{J} > 0$), we showed that the dominance of mass transfer near to the contact line manifests itself in the form of a singularity at $\Theta_0 = 0$ in the contact-line law (3.16), the leading-order contact-line velocity $\dot{S}_0$ being unbounded below as $\Theta_0 \to 0^+$. The relevant initial conditions (3.30) were shown to depend only on the initial width and mass of the two-dimensional symmetric drop, surface tension eradicating at leading order all other details of the initial drop profile during its early-time evolution (over the timescale $t = \mathrm{O}(1)$ as $\lambda \to 0$) to a state in which the mean curvature, and hence the pressure, is constant (at leading order in the thin-film limit).

In Section 4 we showed that, in the distinguished limit in which mass transfer is large in the sense that $J = \mathrm{O}(1)$ as $\lambda \to 0$, contact-line motion occurs on the order-unity timescale $t = \mathrm{O}(1)$ as $\lambda \to 0$, so that the leading-order outer evolution equation for the drop thickness is the full thin-film equation (2.1) without the effects of slip. We note that it is unusual in such thin-film formulations for the time derivative of h_0 to enter the leading-order balance on the timescale of contact-line motion. We showed that the leading-order outer problem selected in the small-slip limit is markedly different depending on whether there is mass loss ($J > 0$) or mass gain ($J < 0$). In the case of mass loss ($J > 0$), we recovered equations (4.11)–(4.12) and showed that the dominance of mass loss at the contact line results in the novel contact-line law (4.5), with the leading-order macroscopic contact angle $\theta_0(t)$ being determined as part of the solution to the leading-order outer problem and with, remarkably, the leading-order outer solution being entirely independent of the microscopic contact angle. However, in the case of mass gain ($J < 0$), we showed that the dominance of mass gain at the contact line results in the additional constraint (4.9) that the macroscopic contact angle be equal to the microscopic one; the resulting novel contact-line law (4.10) reduces the leading-order outer problem from a free-boundary problem to one in which the location of the moving boundary is known *a priori*, with $s_0 = 1 - Jt$. Thus, in both regimes, the usual hydrodynamics of contact-line motion (namely the one in the absence of mass transfer) is dominated by the kinematic effects of mass transfer near the contact line. We closed the leading-order outer formulations by imposing the initial conditions (4.16) inherited from the full thin-film problem. The differences between the leading-order outer problems for mass loss and mass gain were shown to result from the degree of freedom $\theta_0(t)$ being transferred from the outer to the inner region when J changes from positive to negative. We emphasise that the apparent discontinuity in the contact-line law when J changes sign is resolved precisely by the small-$\mathcal{J}$ analysis in Section 3 in the sense that the contact-line law (3.16) describes the smooth transition from the contact-line law (4.5) valid for $J > 0$ to the contact-line law (4.10) valid for $J < 0$. A manifestation of this smooth transition is that the contact-line laws in equations (3.16), (4.5) and (4.10) may be combined into a uniformly valid contact-line law of

https://doi.org/10.1017/S0956792515000364 Published online by Cambridge University Press

the form

$$\dot{s} \sim \frac{\mathcal{V}(\theta, J\ln(1/\lambda))}{\ln(1/\lambda)} \text{ as } \lambda \to 0, \tag{7.1}$$

where θ denotes here the relevant leading-order macroscopic contact angle. The contact-line law (3.16) is universal in the same sense as Tanner's law (depending only logarithmically on the ratio of the length scale of the regularisation of the contact-line singularity to that of the drop), while the contact-line laws (4.5) and (4.10) are universal in an even stronger sense (being independent of any details of the regularisation), each of them holding for other regularisations provided mass transfer does not destroy the mechanism that selects the microscopic contact angle on the length scale of the regularisation. We have shown this to be the case for a generalised slip law, but it is not the case for, for example, the regularisation introduced by [34], which utilises a disjoining pressure and a precursor layer, unless mass transfer is 'turned off' in the precursor layer.

In Section 5 we presented in the case of small mass transfer an asymptotic and numerical analysis of the system (3.4), (3.16) and (3.30) governing the evolution of the drop on the timescale of mass transfer. We found that the evolution may be classified into three regimes depending on the rate of mass transfer, $\mathcal{J}$, and the initial cross-sectional area of the drop in $x > 0$, M, as illustrated in Figure 4(b). For sufficiently large $\mathcal{J}$ or sufficiently small M (regime I), both S_0 and Θ_0 tend to zero with the square-root of the time until extinction. For sufficiently small $\mathcal{J}$ and sufficiently large M (regime II), however, as extinction is approached both Θ_0 and $\dot{S}_0$ tend to non-zero constants depending only on $\mathcal{J}$. Thus, there is a transition from square-root to linear scaling behaviour of the drop width at extinction across the borderline between regimes I and II. For $\mathcal{J} < 0$ (regime III), the long-time attractor is a state in which distances scale linearly with time, with both Θ_0 and $\dot{S}_0$ tending to non-zero constants that depend only on $\mathcal{J}$. Despite our leading-order predictions having an error of $O(1/\ln(1/\lambda))$ as $\lambda \to 0$, we obtained convincing visual agreement with our preliminary numerical simulations of equations (2.1)–(2.2) with $n = 1$ for $\lambda = 10^{-5}$ over the timescale of validity of the small-slip asymptotics. For an intermediate range of values of the rate of mass loss, $\mathcal{J}$, that appears to shrink with λ, our preliminary numerical simulations suggest that, when the drop is sufficiently small that the small-slip asymptotics on the timescale of mass loss no longer pertain, the free surface may form a rim and rapidly touch down at an interior point near to the contact line. In order to gain some insight into the dynamics governing this touchdown phenomenon, which appears to occur only in regime I when surface tension must cope with the macroscopic contact angle tending to zero with the time to extinction on the timescale of mass loss, it may be useful to investigate the evolution near to extinction via more comprehensive numerical simulations and an asymptotic analysis in the small-slip limit of the rapid evolution in the temporal boundary layer just before touchdown. It may also be insightful to apply such methods to investigate the final stages of the evolution just before extinction to establish whether the scaling behaviours exhibited in regimes I and II on the timescale of mass loss pertain all the way up to extinction.

In Section 6, we presented in the case of large mass transfer an asymptotic and numerical analysis of the systems governing the evolution of the drop on the timescale of mass transfer. For both mass loss and gain, we began by reconciling the small-slip asymptotics in Sections 3 and 4 by using a matched-asymptotic analysis to shown that the

https://doi.org/10.1017/S0956792515000364 Published online by Cambridge University Press

small-$|J|$ predictions in Section 6 are in agreement with the corresponding large-$|\mathcal{J}|$ ones in Section 5. In the case of mass loss ($J > 0$), we used the small- and large-J asymptotic analyses in Sections 6.1.1–6.1.2, the near-extinction asymptotic analysis in Section 6.1.4 and our preliminary numerical simulations of (2.1)–(2.2) with $n = 1$ and $\lambda \ll 1$ in Section 6.1.5 to provide convincing evidence that, at leading order in the small-slip limit, the local attractor near extinction is in general the exact solution (6.16) of the leading-order outer problem in which distances scale with the square-root of the time until extinction. In the case of mass gain ($J < 0$), we used the small- and large-$|J|$ asymptotic analyses in Sections 6.2.1–6.2.2 and our preliminary numerical simulations of equations (2.1)–(2.2) with $n = 1$ and $\lambda \ll 1$ in Section 6.2.4 to provide convincing evidence that, at leading order in the small-slip limit, the long-time attractor is the similarity solution in Section 6.2.3 in which distances scale linearly with time. We found that in the case of mass gain, if the rate of change of the curvature of the initial profile is sufficiently large, then our preliminary numerical simulations of equations (2.1)–(2.2) with $n = 1$ and $\lambda \ll 1$ deviate substantially from the leading-order predictions of the small-slip asymptotics in a small window of time near $t = 0$. It may be interesting to gain a better understanding of this surface-tension-driven phenomenon by undertaking, for example, a matched-asymptotic analysis of the regime in which $\lambda \ll 1$ and the rate of change of the curvature of the initial profile is large in a neighbourhood of the contact line.

We note that the aim of our preliminary numerical simulations was rather modest in the sense that we employed them largely to provide quality control for the leading-order asymptotic analyses presented in Sections 3 and 4. We did this by choosing a small value of λ, namely 10^{-5}, and initial conditions that do not vary too dramatically. An important direction for future research may be to ascertain the accuracy of our asymptotic predictions for larger values of λ and for other initial conditions, especially in the case of small mass transfer in which the relevant small parameter depends only logarithmically on λ. However, in doing this it would perhaps be prudent both to refine the modelling assumptions to be application specific and to proceed to second order in the asymptotic analysis before an error analysis is undertaken and before asymptotic predictions are compared with experimental data (the latter for the reasons given in Section 5.2.1).

The generalisation of the small-slip asymptotics in Sections 3 and 4 to three dimensions and to prescribed non-uniform rates of mass transfer of $O(1/\ln(1/\lambda))$ and of $O(1)$ as $\lambda \to 0$ (in which the variation is slow in the sense that it is on the length scale of the contact set and on the timescale of $O(\ln(1/\lambda))$ and of $O(1)$ as $\lambda \to 0$, respectively) are both straightforward, the leading-order inner problem near the contact line being of the same size (i.e. of $O(\lambda)$) and quasi-two-dimensional in each plane perpendicular to the contact line. In more sophisticated models for the evaporation of a sessile liquid drop, such as those considered by [12, 28] and references therein, the mass transfer is coupled to a model for the transport of the liquid vapour away from the drop and may vary on the length scale of the regularisation of the contact-line singularity. The corresponding matched-asymptotic analysis of such models is therefore expected to be significantly more complicated than the one presented here and a worthwhile direction for future research that we hope to be aided by the insight that we have gained. We shall therefore record the three-dimensional leading-order outer formulations in the case of prescribed slowly-varying non-uniform

https://doi.org/10.1017/S0956792515000364 Published online by Cambridge University Press

rates of mass transfer, before commenting briefly on the axisymmetric case relevant to the evaporation of a sessile liquid drop on a planar substrate.

Allowing the rate of mass transfer J to be a prescribed function of position $\mathbf{x}$ in the planar substrate and of time t, the three-dimensional generalisation of the free-boundary problem (2.1)–(2.2) in Section 2 is given by

$$\frac{\partial h}{\partial t} + \nabla \cdot \left((h^3 + \lambda^{3-n} h^n) \nabla \nabla^2 h \right) = -J(\mathbf{x}, t) \text{ in } \Omega(t), \tag{7.2}$$

with

$$h = 0, \ -\frac{\partial h}{\partial \nu} = 1, \ h^n \frac{\partial^3 h}{\partial \nu^3} = 0 \text{ on } \partial\Omega(t), \tag{7.3a-c}$$

where $\Omega(t)$ is the contact set between the liquid and the substrate, whose boundary $\partial\Omega(t)$ forms the contact line and has outward normal derivative $\partial/\partial\nu$ and outward normal velocity v. We note that the boundary condition (7.3c) is automatically satisfied for $2 \leqslant n < 3$, but must be imposed for $n < 2$. The thin-film problem (7.2)–(7.3) is closed by prescribing the initial drop profile and contact set, say $h(\mathbf{x}, 0) = \mathcal{H}(\mathbf{x})$ for $\mathbf{x} \in \Omega(0)$. We note that the expression representing global conservation of mass is given by

$$\frac{\mathrm{d}}{\mathrm{d}t} \left(\iint_{\Omega(t)} h \, \mathrm{d}S \right) = - \iint_{\Omega(t)} J \, \mathrm{d}S. \tag{7.4}$$

In the case of small mass transfer as in Section 3, *i.e.* for $\mathcal{J}(\mathbf{x}, T) = J \ln(1/\lambda) = \mathrm{O}(1)$, on the slow timescale $T = t/\ln(1/\lambda) = \mathrm{O}(1)$ as $\lambda \to 0$, the leading-order outer problem in Section 3.1 becomes

$$\nabla^2 h_0 = -P_0 \text{ in } \Omega_0(T); \quad h_0 = 0, \ -\frac{\partial h_0}{\partial \nu} = \Theta_0 \text{ on } \partial\Omega_0(T), \tag{7.5}$$

the leading-order pressure $P_0(T)$ and macroscopic contact angle $\Theta_0(\mathbf{x}, T)$ being coupled to the evolution of $h_0(\mathbf{x}, T)$ and $\Omega_0(T)$ by the condition for global conservation of mass, namely

$$\frac{\mathrm{d}}{\mathrm{d}T} \left(\iint_{\Omega_0(T)} h_0 \, \mathrm{d}S \right) = - \iint_{\Omega_0(T)} \mathcal{J} \mathrm{d}S, \tag{7.6}$$

as well as the contact-line law

$$V_0 = \mathcal{V}(\Theta_0(\mathbf{x}, T), J(\mathbf{x}, T)) \text{ for } \mathbf{x} \in \partial\Omega_0(T); \tag{7.7}$$

here, V_0 is the outward normal velocity of $\partial\Omega_0(T)$ (with $v \sim V_0/\ln(1/\lambda)$ as $\lambda \to 0$), $\mathcal{V}$ is defined by equation (3.16) and the dependence of $\mathcal{V}$ on its arguments is analysed in Section 3.3. For the same reasons as in the two-dimensional problem, the problem (7.5)–(7.7) is closed by the prescribing the initial location of the contact set to be given by $\Omega_0(0) = \Omega(0)$ and the initial volume of the drop.

In the case of large mass transfer as in Section 4, *i.e.* for $J(\mathbf{x}, t) = \mathrm{O}(1)$, on the order-unity timescale $t = \mathrm{O}(1)$ as $\lambda \to 0$, the leading-order outer problems for mass loss and gain in Section 4.2 become

$$\frac{\partial h_0}{\partial t} + \nabla \cdot \left(h_0^3 \nabla \nabla^2 h_0 \right) = -J(\mathbf{x}, t) \text{ in } \Omega_0(t); \quad h_0 = 0, \ -\frac{\partial h_0}{\partial \nu} = \theta_0 \text{ on } \partial\Omega_0(t); \tag{7.8}$$

https://doi.org/10.1017/S0956792515000364 Published online by Cambridge University Press

in the case of mass loss ($J > 0$), the contact-line velocity $v \sim v_0$ as $\lambda \to 0$, with

$$\text{for } J < 0, \quad v_0 = -\frac{J(\mathbf{x}, t)}{\theta_0(\mathbf{x}, t)} \text{ for } \mathbf{x} \in \partial\Omega_0(t), \tag{7.9}$$

where the leading-order macroscopic contact angle $\theta_0(\mathbf{x}, t)$ is determined as part of the solution; in the case of mass gain ($J < 0$), the macroscopic contact angle is equal to the microscopic one and the contact-line velocity is equal to the local rate of mass gain, i.e.

$$\text{for } J < 0, \quad \theta_0(\mathbf{x}, t) = 1, \ v_0 = -J(\mathbf{x}, t) \text{ for } \mathbf{x} \in \partial\Omega_0(t). \tag{7.10}$$

In both cases, the leading-order outer formulation is closed by imposing on Ω_0 and h_0 the same initial conditions as for Ω and h.

All of the analysis presented in this paper for a two-dimensional drop carries over in the usual way to the case of a three-dimensional axisymmetric drop subjected to a uniform rate of mass transfer. For example, in the case of small uniform mass transfer governed by equations (7.5)–(7.7), the regime diagram is qualitatively the same as in Figure 4(b) upon identifying M with the initial volume of the drop; while in the case of large uniform mass loss governed by equations (7.8)–(7.9), the free surface in the axisymmetric version of the two-dimensional exact solution (6.16) is a paraboloid moving with speed J normal to, and toward, the substrate. We note that, more generally, in the three-dimensional case of large uniform mass loss governed by equations (7.8)–(7.9), $h_0 = \mathcal{H}(\mathbf{x}) - Jt$ is an exact solution in which the contact line is given by the level set $\mathcal{H}(\mathbf{x}) = Jt$ for all profiles $\mathcal{H}(\mathbf{x})$ with constant mean curvature (at leading order in the thin-film limit, so that $\nabla^2\mathcal{H}$ is a negative constant). However, by analogy with the two-dimensional symmetric case (in which surface tension drives the initial film profile toward a surface of constant mean curvature), we expect the axisymmetric three-dimensional exact solution to be, at leading order in the small-slip limit and in general, the local attractor near extinction. These predictions are consistent with numerous experimental studies: for example, [5, 9, 32, 36] report that, for a variety of liquids, the radius of the circular contact set of an evaporating axisymmetric sessile liquid drop exhibits near to extinction an approximately square-root scaling behaviour with the time to extinction. Usually the presence of this "D^2-law" is taken to be indicative of diffusion-limited kinetics [13]. Our analysis demonstrates that the intricacies of contact-line motion coupled to mass loss can give similar behaviour, albeit with dramatically simplified physics.

Acknowledgements

This publication is based on work supported in part by Award No KUK-C1-013-04, made by King Abdullah University of Science and Technology (KAUST). We are grateful to Dr Erqiang Li, Professor Sigurdur D. Thoroddsen, Professor John S. Wettlaufer and Professor Thomas P. Witelski for useful discussions on this work. The authors would like to dedicate this work to Professor John R. Ockendon on the occasion of his 75th Birthday. As his research student, JMO was supported, inspired and energised by John to pursue a research career in free-boundary problems. Thank you.

References

[1] Ajaev, V. S. (2005) Spreading of thin volatile liquid droplets on uniformly heated surfaces. *J. Fluid Mech.* **528**, 279.

[2] Anderson, D. M. & Davis, S. H. (1995) The spreading of volatile liquid droplets on heated surfaces. *Phys. Fluids* **7**, 248.

[3] Bonn, D., Eggers, J., Indekeu, J., Meunier, J. & Rolley, E. (2009) Wetting and spreading. *Rev. Mod. Phys.* **81**, 739.

[4] Burelbach, J. P., Bankoff, S. G. & Davis, S. H. (1988) Nonlinear stability of evaporating/condensing liquid films. *J. Fluid Mech.* **195**, 463.

[5] Cachile, M., Bénichou, O., Poulard, C. & Cazabat, A. M. (2002) Evaporating droplets. *Langmuir* **18**, 8070.

[6] Cazabat, A. M. & Guéna, G. (2010) Evaporation of macroscopic sessile droplets. *Soft Matter* **6**, 2591.

[7] Davis, S. H. & Hocking, L. M. (2000) Spreading and imbibition of viscous liquid on a porous base. *Phys. Fluids* **12**(7), 1646.

[8] Deegan, R. D., Bakajin, O., Dupont, T. F., Huber, G., Nagel, S. R. & Witten, T. A. (1997) Capillary flow as the cause of ring stains from dried liquid drops. *Nature* **389**, 827.

[9] Deegan, R. D., Bakajin, O., Dupont, T. F., Huber, G., Nagel, S. R. & Witten, T. A. (2000) Contact line deposits in an evaporating drop. *Phys. Rev. E* **62**, 756.

[10] Dunn, G. J., Wilson, S. K., Duffy, B. R., David, S. & Sefiane, K. (2008) A mathematical model for the evaporation of a thin sessile liquid droplet: Comparison between experiment and theory. *Colloids Surf. A* **323**, 50.

[11] Dunn, G. J., Wilson, S. K., Duffy, B. R., David, S. & Sefiane, K. (2009) The strong influence of substrate conductivity on droplet evaporation. *J. Fluid Mech.* **623**, 329.

[12] Eggers, J. & Pismen, L. (2010) Nonlocal description of evaporating drops. *Phys. Fluids* **22**(11), 112101.

[13] Erbil, H. Y., McHale, G. & Newton, M. I. (2002) Drop evaporation on solid surfaces: Constant contact angle mode. *Langmuir* **18**, 2636.

[14] Eriksson, K., Estep, D., Hansbo, P. & Johnson, C. (1996) *Computational Differential Equations*, Cambridge University Press, University Printing House, Cambridge, CB2 8BS, UK.

[15] Fried, E. & Jabbour, M. (2012) Dynamical equations for the contact line of an evaporating or condensing sessile drop. *J. Fluid Mech.* **703**, 204.

[16] Gelderblom, H., Bloemen, O. & Snoeijer, J. H. (2012) Stokes flow near the contact line of an evaporating drop. *J. Fluid Mech.* **709**, 69.

[17] Greenspan, H. P. (1978) On the motion of a small viscous droplet that wets a surface. *J. Fluid Mech.* **84**, 125.

[18] Hocking, L. M. (1976) A moving fluid interface on a rough surface. *J. Fluid Mech.* **76**(4), 801.

[19] Hocking, L. M. (1983) The spreading of a thin drop by gravity and capillarity. *Q. J. Mech. Appl. Math.* **36**, 55.

[20] Hocking, L. M. (1995) On contact angles in evaporating liquids. *Phys. Fluids* **7**, 2950.

[21] Hocking, L. M. & Rivers, A. D. (1982) The spreading of a drop by capillary action. *J. Fluid Mech.* **121**, 425–442.

[22] Huh, C. & Scriven, L. E. (1971) Hydrodynamic model of steady movement of a solid/liquid/fluid contact line. *J. Colloid Interface Sci.* **35**(1), 85.

[23] King, J. R. (2001) Thin-film flows and high-order degenerate parabolic equations. In: A. C. King & Y. D. Shikhmurzaev (editors), *IUTAM Symposium on Free Surface Flows*, Kluwer, Dordrecht, pp. 7–18.

[24] King, J. R. & Bowen, M. (2001) Moving boundary problems and non-uniqueness for the thin film equation. *Eur. J. Appl. Math.* **12**, 321.

[25] King, J. R. & Oliver, J. M. (2005) Thin-film modelling of poroviscous free surface flows. *Eur. J. Appl. Math.* **15**, 519.

[26] Lacey, A. A. (1982) The motion with slip of a thin viscous droplet over a solid surface. *Stud. Appl. Math.* **67**, 217.
[27] Murisic, N. & Kondic, L. (2008) Modeling evaporation of sessile drops with moving contact lines. *Phys. Rev. E* **78**, 065301.
[28] Murisic, N. & Kondic, L. (2011) On evaporation of sessile drops with moving contact lines. *J. Fluid Mech.* **679**, 219.
[29] Myers, T. G. (1998) Thin films with high surface tension. *SIAM Rev.* **40**, 441.
[30] Oron, A., Davis, S. H. & Bankoff, S. G. (1997) Long-scale evolution of thin liquid films. *Rev. Mod. Phys.* **69**, 931.
[31] Plawsky, J. L., Ojha, M., Chatterjee, A. & Wayner Jr, P. C. (2008) Review of the effects of surface topography, surface chemistry, and fluid physics on evaporation at the contact line. *Chem. Eng. Comm.* **196**, 658.
[32] Poulard, C., Benichou, O. & Cazabat, A. M. (2003) Freely receding evaporating droplets. *Langmuir* **19**, 8828.
[33] Poulard, C., Guéna, G., Cazabat, A. M., Boudaoud, A. & Ben Amar, M. (2005) Rescaling the dynamics of evaporating drops. *Langmuir* **21**, 8226.
[34] Schwartz, L. W. & Eley, R. R. (1998) Simulation of droplet motion on low-energy and heterogeneous surfaces. *J. Colloid Interface Sci.* **202**, 173.
[35] Sefiane, K. & Ward, C. A. (2007) Recent advances on thermocapillary flows and interfacial conditions during the evaporation of liquids. *Adv. Colloid Interface Sci.* **134**, 201.
[36] Shahidzadeh-Bonn, N., Rafaï, S., Azouni, A. & Bonn, D. (2006) Evaporating droplets. *J. Fluid Mech.* **549**, 307.
[37] Shampine, L. F. (2007) Accurate numerical derivatives in MATLAB. *ACM Trans. Math. Softw.* **33**(4).
[38] Sodtke, C., Ajaev, V. S. & Stephan, P. (2007) Evaporation of thin liquid droplets on heated surfaces. *Heat Mass Transfer* **43**, 649.
[39] Tanner, L. H. (1979) The spreading of silicone oil drops on horizontal surfaces. *J. Phys. D: Appl. Phys.* **12**, 1473.
[40] Voinov, O. V. (1976) Hydrodynamics of wetting. *Fluid Dyn.* **11**, 714.
[41] Ward, J. P. & King, J. R. (2012) Thin-film modelling of biofilm growth and quorum sensing. *J. Eng. Math.* **73**, 71.
[42] Zhornitskaya, L. & Bertozzi, A. L. (2000) Positivity-preserving numerical schemes for lubrication-type equations. *SIAM J. Numer.* **37**(2), 523.